SYNTHESIS AND CHARACTERIZATION OF MESOPOROUS CERIA-ZIRCONIA SOLID SOLUTION

A project report
submitted in partial fulfilment of the requirements
for the award of the degree of

MASTER OF TECHNOLOGY

in

CHEMICAL ENGINEERING

SPECIALISATION : CATALYSIS TECHNOLOGY

by

SOURAV KHAN
(CH09M005)

Under the guidance of
PROF. P. SELVAM

DEPARTMENT OF CHEMICAL ENGINEERING
INDIAN INSTITUTE OF TECHNOLOGY- MADRAS
CHENNAI 600 036

MAY 2011

THESIS CERTIFICATE

This is to certify that the thesis titled "**SYNTHESIS AND CHARACTERIZATION OF CERIA-ZIRCONIA SOLID SOLUTION**", submitted by **Mr. Sourav Khan** to the Indian Institute of Technology-Madras, Chennai for the award of the degree of **Master of Technology in Catalysis Technology (Chemical Engineering)**, is a *bona-fide* record of the research work done by him under our supervision. The contents of this thesis, in full or in parts, have not been submitted to any other Institute or University for the award of any degree or diploma.

Guide

PROF. P. SELVAM
National Centre for Catalysis Research
Department of Chemistry
IIT Madras, Chennai 600 036

Co-Guide

Dr. PREETI AGHALAYAM
Department of Chemical Engineering
IIT Madras, Chennai 600 036

Place: CHENNAI

Date :

ACKNOWLEDGEMENTS

First of all I would like to express my gratitude to my research guide **Prof. P. Selvam** for his support, advice, valuable discussions constant encouragement, critical ideas, invaluable suggestions and unfailing guidance during the course of the whole research work presented in this thesis. He has always a lot of good ideas, many of which nobody else has ever thought of. What is still better is that he always has the time to discuss these. I am always indebted to him. I have been able to learn a great deal from him and consider my association is a rewarding experience for me. I thank him for his patient guidance, open discussions, unbounded enthusiasm and interest.

I express my sincere gratitude to **Prof. B. Viswanathan** for his inspiring, invaluable guidance, constant encouragement and thought provoking discussions. I am really grateful to him for providing opportunities to learn various aspects in catalysis. It is my privilege to express my gratitude to him for introducing me to the field of catalysis.

I am very much grateful to **Dr. Preeti Aghalayam,** my research co-guide, for her constant encouragement, support and invaluable suggestions.

I sincerely thank all my PG committee members, **Dr. S. Sivasanker**, **Prof. R. Ramnarayanan, Dr. K.R. Krishnamurthy**, for their constant encouragement and suggestions

I express my deep gratitude to **Prof. S. Pushpavanam**, Head, Department of Chemical Engineering and other faculty members of our department for the support and facilities provided in carrying out this project work.

I am thankful to **National Centre for Catalysis Research (NCCR)** where in I have carried out most of my research work. I owe a great debt to **IIT Madras** for providing the state-of-the-art facilities for carrying out my research work.

ABSTRACT

Mesoporous Ceria-Zirconia solid composite have attracted considerable interest owing to their broad range of applications in various fields, ranging from catalysis to high- performance transformation-toughened structural engineering ceramics, solid oxide fuel cell (SOFC), gas sensors, electro-optical materials fabrication, damage-resistant optical coatings, gate dielectrics etc., in addition to the classical application in the so-called three way catalysts (TWC) for automotive exhaust treatment. The important property that makes mesoporous ceria as an excellent catalytic material is its oxygen storage and release capacity (OSC) via the redox shift between Ce^{4+} and Ce^{3+} under oxidizing and reducing conditions, respectively. But mesoporous ceria has poor thermal stability and known to sinter at high temperatures, which leads to catalytic deactivation. Therefore, much effort has been devoted in recent years to design suitable mesoporous CeO_2-based composite systems, which can enhance the thermal stability of ceria without diminishing its special features, such as its unique redox properties and its high oxygen mobility. Moreover, the redox and catalytic properties of mesoporous ceria and its composite oxides are dependent upon some other factors, which include crystallite size, phase modification, and morphology. In addition, fine tuning of the particle size of a catalyst in nanometer scale results in increasing the specific surface area, narrow pore size distribution, highly ordered channels, thus improving catalytic performance. Ceria easily forms solid solutions with other transitional-metals and rare-earth elements. Especially, solid solutions of ceria with Group IV transitional-metals deserve particular attention for their applicability in various technologically important catalytic processes. Mesoporous CeO_2-ZrO_2 solid solutions have been employed in various reactions which include CO oxidation, shoot oxidation, water-gas shift reaction, and so on. Therefore, it was interesting to investigate the structural and catalytic properties of novel mesoporous ceria-zirconia composite.

In order to exploit them without losing their unique features, it is very essential to synthesize these mesoporous nanocomposites. The unique feature for the synthesis of mesoporous materials is focused on the use of supramolecular assembly of template molecules as structure-directing agent. The soft templates such as triblock copolymers or surfactants, which

form the self-aggregated superstructures in solution phase, play the key role in directing the formation of organized porous structures. Nonsiliceous mesoporous materials are often more difficult to synthesize by precipitation routes and often exhibit poor crystallinity and low thermal stability. In this present investigation, mesoporous ceria, mesoporous zirconia and mesoporous ceria-zirconia solid solutions possessing high specific surface area, better thermal stability are synthesized. The thermal and structural stability of the mesoporous ceria-zirconia solid solutions are strongly influenced by the synthetic methodology.

Generally, there exist two main methods for the preparation of mesoporous metal oxides; the conventional one is the so-called soft-templating method, which employs surfactants to form micelles in aqueous solutions, and then allows for a lot of mesoporous metal oxides and mixed oxides to be synthesized. However, many mesoporous metal oxides prepared in this way have a lot of disadvantages which include amorphous inorganic walls, poor mesoporous structure, and thermal instability during the removal of organic templates, which greatly limited their applications to catalyst and other functional nanomaterials .The synthesis strategy adopted here for improving themal stability and also the microtexture of the mesoporous ceria-zirconia composite is based on a sol-gel process combined with evaporation-induced self-assembly (EISA) in ethanol using neutral tri-block copolymer as the template. Another method is the nanocasting strategy where the pores and channels of mesoporous silica are infiltrated with suitable precursors and then the mixture was subjected to heat treatment at a certain temperature to convert the precursors to oxides. After the final selective removal of the inorganic templates, the shape-reversed molded structures may be obtained. All the samples were systematically characterized using various analytical and spectroscopic tecniques. In conclusion, nanocasting and soft templating routes were successfully used for the synthesis of mesoporous ceria, zirconia and ceria-zirconia composites. Physico-chemical characterization of all these materials showed that they are thermally stable; possess high surface area and excellent textural properties. Finally, for the first-time, we have established mesoporous ceria-zirconia solid solution that the unit cell parameters vary linearly with composition in accordance with Vegard's law.

KEYWORDS: Mesoporous ceria and zirconia; Mesoporous ceria-zirconia solid solution, Oxygen storage capacity.

TABLE OF CONTENTS

LIST OF TABLES

LIST OF FIGURES

x

ABBREVIATIONS

Ce	Cerium
EDAX	Energy Dispersive X-Ray Analysis
FDHM	Full Width at Half Maximum
SEM	Scanning Electron Microscopy
TEM	Transmission Electron Microscopy
TGA	Thermo Gravimetric Analysis
UV-Vis	Ultraviolet – Visible Spectroscopy
XRD	X-ray Diffraction
Zr	Zircoium

NOTATIONS

Å	Angstrom
θ	Angle
cm	centimeter
K	Degree Kelvin
°C	Degree Celsius
h	Hour
T	Temperature
λ	Wavelength

CHAPTER 1

INTRODUCTION

1.1 MESOPOROUS METAL OXIDES

Mesoporous materials with regular geometries have been recently paid much attention owing to their scientific importance and great potentials in practical applications such as catalysis, adsorption, sensing, and fuel cells. Pore sizes of mesoporous materials allow not only an easy accessibility for molecules with sizes up to a certain range but also a possible controllability in functions depending on the pore geometries. Well-ordered mesoporous non-siliceous metal oxides have attracted significant attention in recent years because of their excellent textural characteristics such as high surface area, large pore volume, uniform pore size distribution, high thermal and hydrothermal stability.

The chemistry of non-siliceous materials is much more diverse than that of the siliceous ordered mesoporous oxides, and thus, the synthesis strategies for their production need to be more diverse. Among the widely studied transition metal oxides, zirconia is of particular interest because it possesses both acidic and basic surface active sites, excellent ion exchange capacity and rich surface oxygen defects, which provide multi-functionalities common in catalysis (Liu et al., 2008). Because of their excellent chemical resistance, refractory character, oxygen ion conductivity and polymorphous nature, mesoporous ZrO_2-based oxides have found application in a wide range of technologies, including automotive three-way exhaust catalysis, solid oxide fuel cells (SOFCs) and gas sensors (Liu and Baker, 2008). Without doubt, the poor ther mal stability of mesoporous zirconia will severely limit its practical applications such as in the high temperature catalytic reactions or fuel cells.

CeO_2 is of particular interest due to its catalytic activity, high oxygen storage and release ability; has been widely used in three-way catalysts for automobile exhaust, for the oxidation of different hydrocarbons, adsorbent for removal of organics from polluted water, and in solid oxide fuel cells (Wang et al., 2010). However, the basic requirement for many applications of

these materials is the preparation, which is not only reproducible on the nano–scale but also with a high surface area, tailored structure and morphology. Ceria–zirconia solid solutions are very important material for auto-exhaust catalysis (TWC) and oxygen sensors. This solid solution is known to work effectively benefitting the advantage of large oxygen storage/release capacity of ceria because of the reversible reaction of Ce^{4+} to Ce^{3+} Ceria, however, lacks high temperature stability, a problem which is solved through adding zirconia to ceria lattice as shown in Figure 1.1. Incorporation of zirconium, also, reduces the electrical resistivity of the material making it more adequate for oxygen sensing (Ghom et al., 2009).
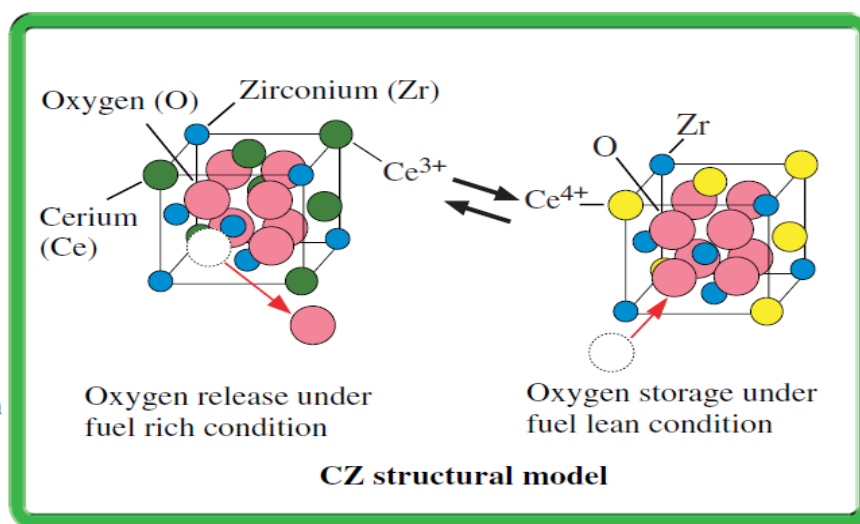
Figure 1.1: Mechanism of oxygen storage and release (R&D Review of Toyota).

1.2. SYNTHESIS PATHWAYS TO MESOPOROUS METAL OXIDES

A variety of methodologies for synthesizing mesoporous metal oxides have been investigated such as nanocasting (replica) method, evaporation-induced self-assembly (EISA) method, sol–gel method, hydrothermal method. However, mesoporous metal oxides prepared from the so called chemical soft templating method suffered from a lot of disadvantages, such as amorphous walls, poor mesoporous structure, and thermal instability during the removal of organic templates, which greatly limited their applications as catalyst and other functional nanomaterials (Wang et al., 2010).

Figure 1.2: Historical flow in synthesis strategies of mesoporous materials: (a) template synthesis, (b) replica route, and (c) elemental substitution .(Advances in Nanoporous Materials.)

The high thermal stability of mesoporous phases is perhaps the most critical requirement for their use in several functional applications (Carreon et al., 2005). In general, the thermal stability of mesostructured metal oxide phases will depend on:

(a) Degree of charge-matching at the organic–inorganic interface,

(b) Interaction strength between inorganic species and surfactant head-groups,

(c) Tamman temperature of the metal oxide,

(d) Flexibility of the M–O–M bond angles in the constituent metal oxides, and

(e) Occurrence of redox reactions in the metal oxide wall.

The charge matching at the organic–inorganic interface generally allows control over the wall composition, and facilitates cross-linking of the inorganic species into a robust mesostructured framework. The presence of strong covalent bonds between metal oxide species and surfactant head-groups, for example metal–N bonds, means that harsh conditions, such as combustion, are required for surface removal, leading typically to collapse of the mesostructure. On the contrary, metal oxide species should possess low lattice mobility at elevated temperatures in order to prevent transformation of the mesostructured metal oxides into more thermodynamically stable dense phases. The mobility of metal ions or atoms in a crystalline

3

metal oxide increases considerably in the vicinity of its Tamman temperature (defined as 0.5–0.52 Tm, where Tm is the metal oxide melting point. Therefore, the low Tamman temperature of several transition metal oxides (i.e., V_2O_5 472 K, MoO_3 534 K, WO_3 873 K, Nb_2O_5 892 K, Fe_2O_3 919 K, MnO 962 K, TiO_2 1064 K, NiO 1129 K, ZrO_2 1492 K, MgO 1563 K) translates into a limited thermal stability of the corresponding mesostructures. Non-flexible M–O–M bond angles that are unable to accommodate the curvature of the inorganic–organic interface may result in the formation of only lamellar or dense metal oxide phases. Finally, the structural collapse of mesophases may be caused by redox reactions occurring in the metal oxide wall during surfactant removal or catalytic reaction (Yang et al., 1998).

A large number of studies have been carried out to investigate the formation and assembly of mesostructures on the basis of surfactant self-assembly. The initial liquid-crystal template mechanism first proposed by Mobil's scientists is essentially always "true", because the pathways basically include almost all possibilities. Two main pathways, that is, cooperative self-assembly and "true" liquid-crystal templating processes, seem to be effective in the synthesis of ordered mesostructures, as shown in Figure 1.3. Liquid crystalline mesophases can also be prepared in non-aqueous solution. Using ethanolic solutions of non-ionic block copolymers as a medium, Zhao et al., for example, have developed a route by which mesoporous metal oxides can readily be prepared. This appears to be one of the most promising routes to the formation of non-silica mesoporous solids. Soft-templating is defined as a process in which organic molecules serve as a 'mold' and around which a framework is built up. The removal of these organic molecules results in a cavity which retains the same morphology and structure of the organic molecule (Wan and Zhao, 2007). For control over the synthesis of mesoporous solids, the key is to understand the interactions of micellar surfactants with condensable inorganic framework-building units. The following sections review some of the recent methods employed for the synthesis of mesoporous ceria and zirconia and their solid solution (He et al., 2002).
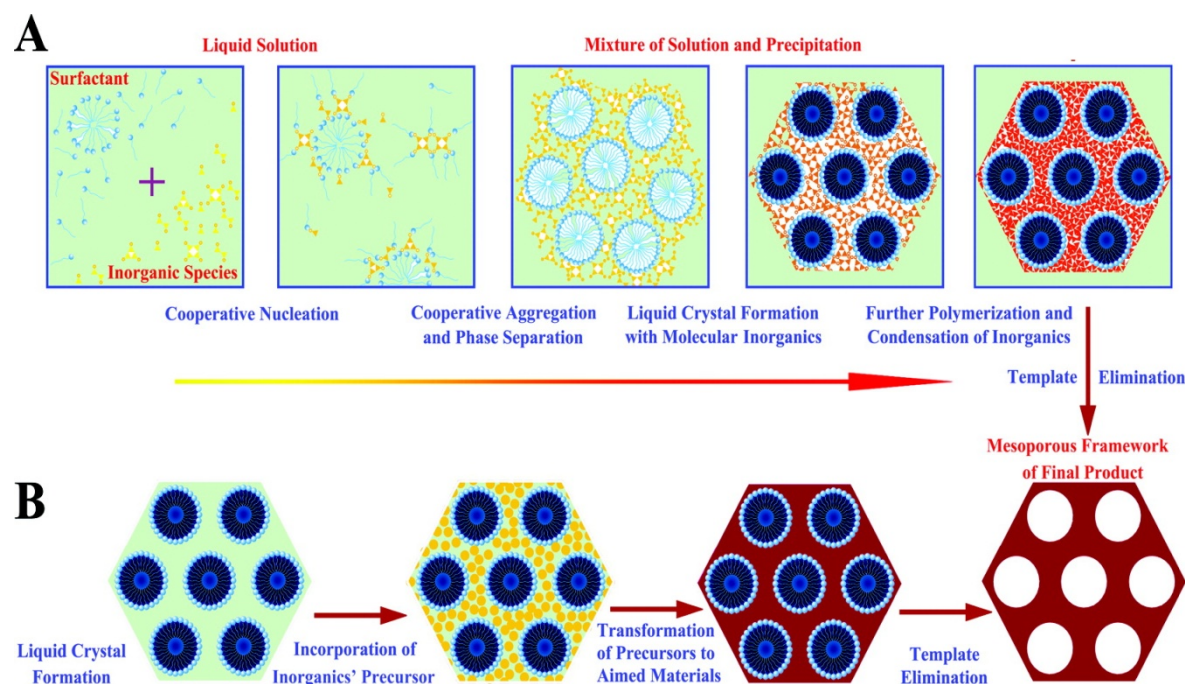
Figure 1.3: Two synthetic strategies of mesoporous materials: (A) co-operative self-assembly; (B) "true" liquid-crystal templating process (Wan and Zhao, 2007).

1.2.1. Evaporation Induced Self Assembly (EISA) Method

EISA is a well-suited approach to prepare ordered mesoporous metal oxides. Self assembly is defined as spontaneous reversible organization of materials by means of non-covalent interaction mainly through hydrogen bonding, Vander Waals forces, and electrostatic forces without any external influence. The evaporation-induced self assembly (EISA) denomination was coined by Brinker et al. to encompass the synthesis methods leading to ordered hybrid mesophases from dilute solutions, upon solvent evaporation. When preparing mesostructured metal oxides, via EISA, several parameters that influence the self-assembly process may be considered. Sanchez's group divided these parameters in two categories: (a) the chemical parameters, related to sol–gel hydrolysis–condensation reactions and relative quantities of surfactant and inorganic precursor; and (b) the processing parameters related to the diffusion of alcohol or tetra hydro Furan (THF).The formation of the mesostructure is favoured when neutral templates such as block copolymers are combined with inorganic precursor solutions in the vicinity of the isoelectric point. When the surfactant concentration reaches the critical micelle

concentration leading to the formation of micelles with the subsequent formation of the organized mesostructure (Cagnol et al., 2003). It has been demonstrated that the critical processing parameter for the formation of ordered mesostructures is the relative humidity (RH). The formation of diverse mesophases by EISA strongly depends on the kinetics of competitive processes of condensation versus organization (Soler-Illia et al., 2002).
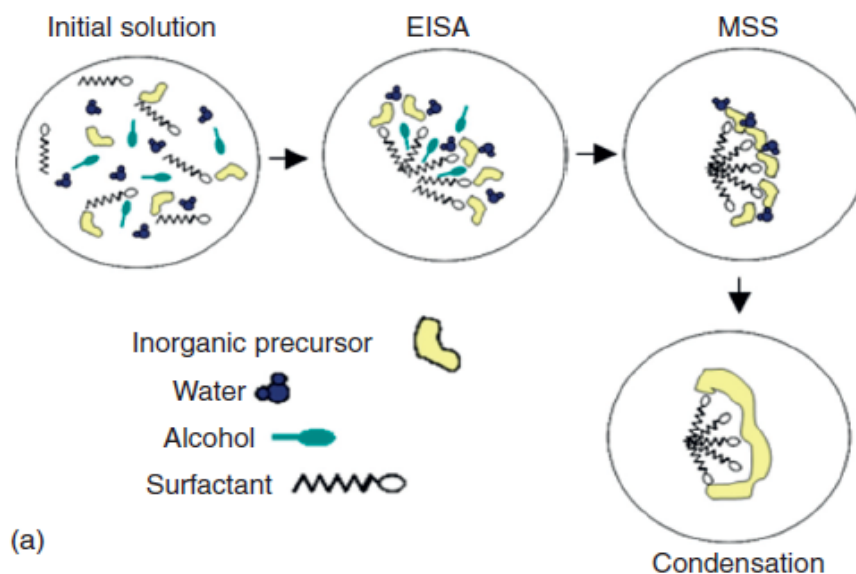
Figure 1.4: (a) Schematic representation of evaporation-induced-self-assembly for the preparation of long-range ordered mesostructures (Brinker et al., 1999).

Figure 1.4 summarizes the steps involved in the organization of ordered periodic mesostructures. The initial solution contains the inorganic species, surfactant, and volatile components. As the evaporation of volatiles proceeds, surfactant concentration increases, and it aggregates to form micellar structures above the critical micelle concentration (Hurd et al., 2001). When the mesostructure is initially formed, the inorganic framework is not fully condensed, and the control of the final mesostructure can be adjusted by modifying the RH conditions (i.e., water molecules can diffuse in and out of the film). At this point, the flexible mesostructure experiences a transition state known as modulable steady state (MSS). Finally, the inorganic framework fully condenses, forming the final mesostructure. The resultant as-synthesized mesostructure is treated thermally to eliminate the organic structure directing agents. This step is used to stabilize the inorganic framework and to obtain the open porous

mesostructure. Calcination temperatures will depend on the decomposition temperature of the structure directing agent. Typical values are in the 300–500 °C range. Alternatively, the structure directing agents can be eliminated by solvent extraction or ultraviolet photodegradation (Clark et al., 2000).

EISA can be considered an LCT-based method (after solvent evaporation, a hybrid LC phase is formed) (Guliants et al., 2004). Starting from solutions below the critical micellar concentration permits one to obtain thin films or gels (Figure 1.5) with excellent homogeneity (high dilution discouraging inorganic polymerization). This method is particularly interesting to work with non-silica systems, where condensation has to be thoroughly controlled (Soler-Illia et al., 2003). The surfactants generally used are Pluronic: P-127 and P-123. (Lu et al., 2000)
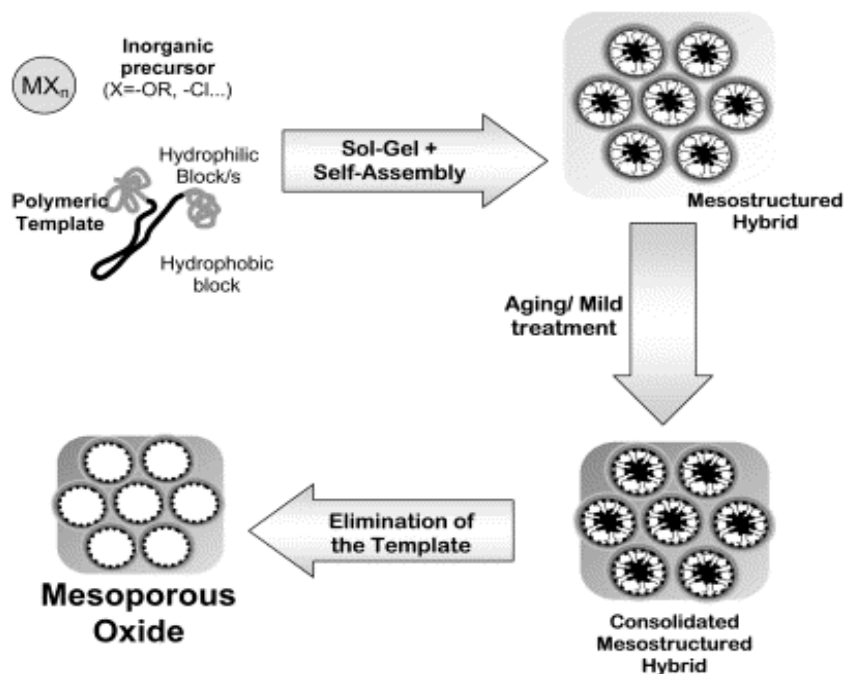
Figure 1.5: Schematic view of the steps leading from composite solution to mesoporous oxide (.Soler-Illia et al., 2003)

For the facile synthesis of ceria-zirconia solid solution with highly ordered mesoporous structures EISA procedure was adopted and the schematic representation is depicted in Figure 1.6.
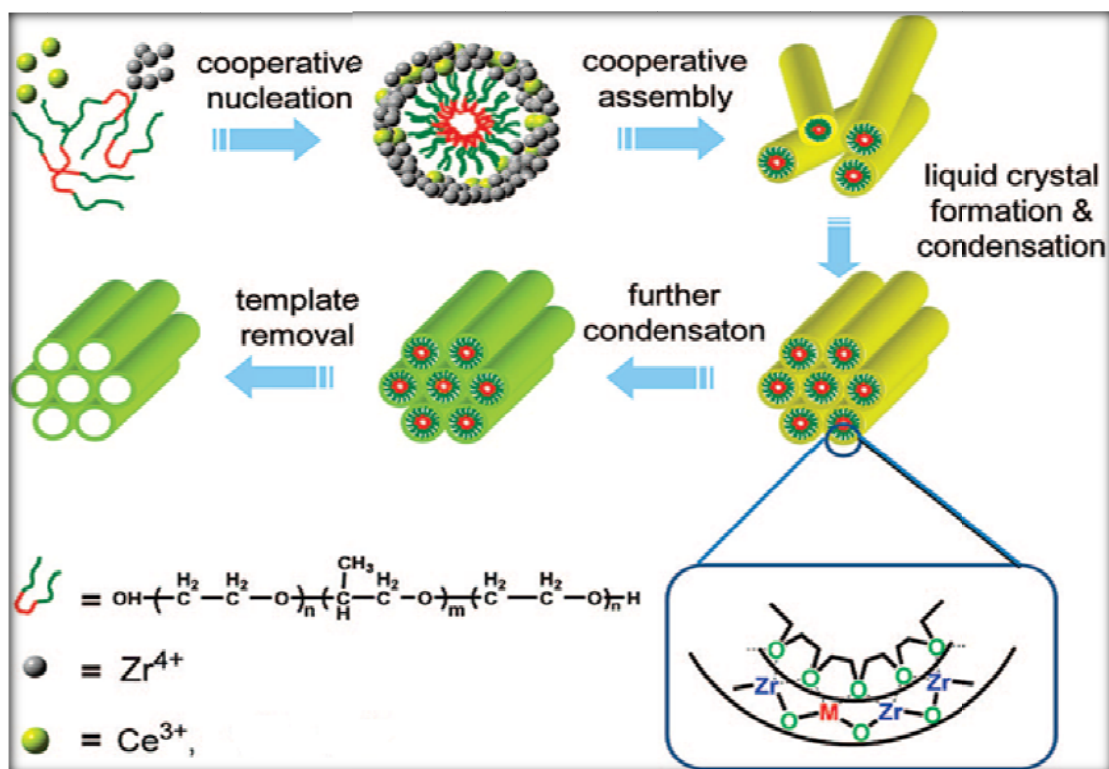
Figure 1.6: Schematic representation of the EISA procedure adopted for preparing ordered mesoporous $Ce_{1-2x}Zr_xO_2$ (Yuan et al.,2009).

1.2.2. Nanocasting Method

Nanocasting or replica method is generally used for the synthesis of mesoporous materials where regular structures of mesoporous materials are replicated into chemically different mesoporous materials with the structural replicate of the template used. Nanocasting is a process used to infiltrate a fluid precursor into the nanometer-sized pore channels of the hard templates, to convert the precursor by the nanostructure confinement into a target nanomaterial that duplicates the morphology and structure of the template, and finally to remove the template. Various inorganic materials, including silica nanoparticles (silica sol), zeolites, anodic alumina membranes, and mesoporous silica materials, have been used as templates (Lu and Schuth, 2010).

SBA-15 is mesoporous siliceous material which exhibits very good textural properties. It is formed using non-ionic triblock co-polymers, generally poly(ethylene oxide)–poly(propylene

8

oxide)–poly(ethylene oxide); $EO_{20}PO_{70}EO_{20}$ (PEO-PPO-PEO; P-123) as shown below in Figure 1.7. SBA-15 is generally used as hard template because of the presence of interconnecting porosity which is required for successful replication (Vartuli et al., 1994).
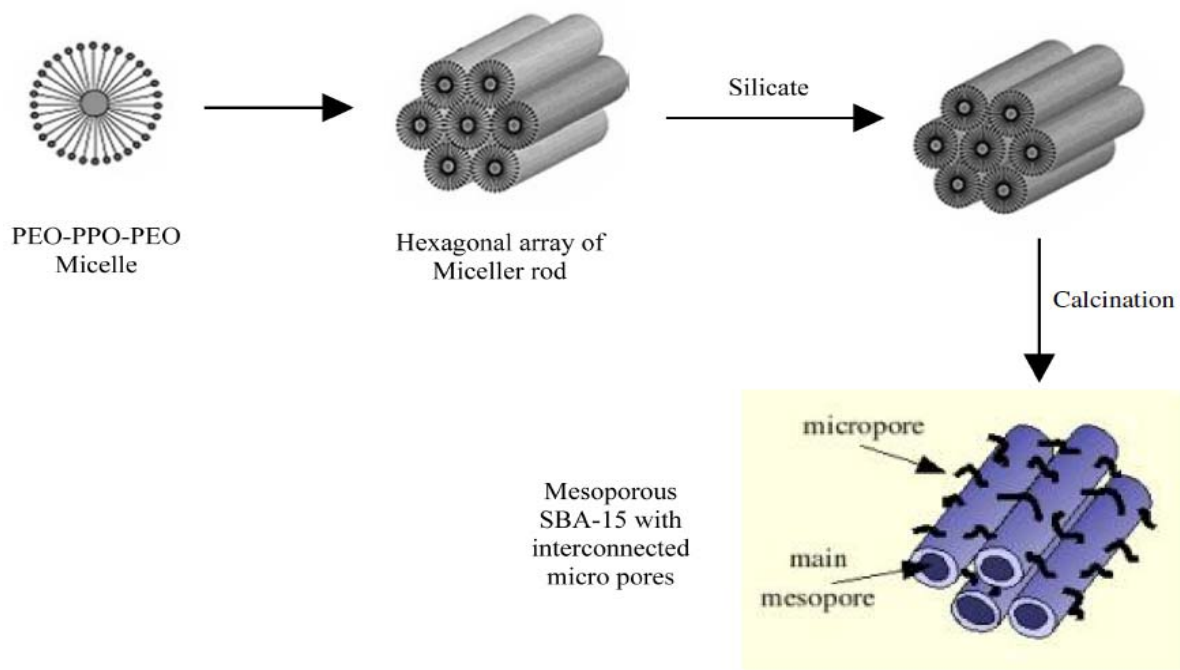
Figure 1.7: Mechanistic pathway for the formation of SBA-15

In this route, the pores of the mesoporous starting material are first filled with inorganic precursors. The precursors inside the pores are converted to the desired final composition, for example, by a heating step and the parent template material is removed, usually by dissolution, to leave a mesoporous structure with a negative replica structure (Figure 1.8) of the desired composition. This route was pioneered by Ryoo and co-workers, who demonstrated the synthesis of a series of mesoporous carbons (CMK series) using different mesoporous silicas as hard templates. Later, it was widely used to prepare mesoporous nonsiliceous materials, such as ZrO_2 CeO_2, Cr_2O_3, MnO_2, NiO, Co_3O_4 and Fe_2O_3 (Liu et al., 2008). Mesoporous metal oxides with 1-D to 3-D structures were prepared by using SBA-15, FDU-5, KIT-6, and SBA-16.

In order to obtain highly ordered mesostructures by this hard template route, the following four requirements should be considered. Firstly, the mesoporous templates should possess high order and a durable thermal stability. Secondly, a full impregnation of the desired precursors

9

within the voids of templates is necessary and such precursors should be easily converted to the desired solid structures with as little volume shrinkage as possible. Thirdly, the mother templates should be facilely and completely removed in order to achieve a faithful replica. Fourthly, in order to control the morphology of the replica of hard templates, the morphology of mesoporous templates should be controlled (Yue et al., 2009) The greatest problem with this method is that silica cannot be removed completely from the product.
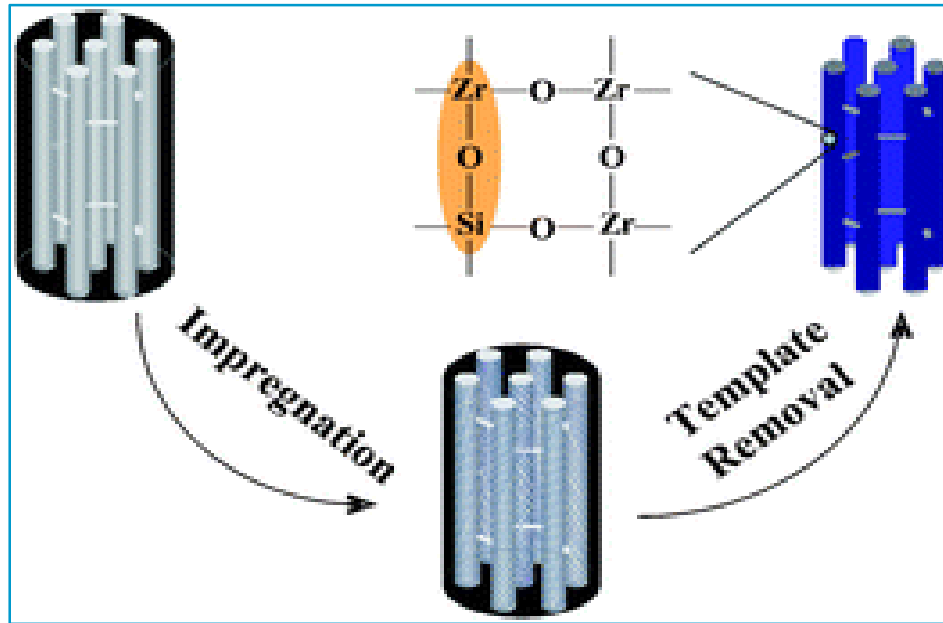
Figure1. 8: Schematic representation of the replica process (Liu and Baker, 2008).

1.3. OXYGEN STORAGE MATERIALS

The definition of the oxygen storage capacity (OSC) is the capability to store and release oxygen. Equation (1.1) presents a very simplified picture of the redox behavior of CeO_2.

$$CeO_2 \leftrightarrow CeO_{2-x} + \tfrac{1}{2} O_2 \qquad\qquad (1.1)$$
$$Ce^{4+} \leftrightarrow Ce^{3+}$$

According to equation (1.1), the oxygen storage is formally considered as the amount of oxygen released (left to right) or stored (right to left) under the net reducing/net oxidizing

conditions. From the thermodynamic point of view, the standard potential for reduction of Ce^{4+} to Ce^{3+} is 1.74 V in solution, which indicates that Ce(IV) in solution is a strong oxidant. In the solid state, the situation is different. CeO_2 crystallizes in the fluorite structure in which each cerium ion is co-ordinated by eight oxygen neighbours. This coordination stabilizes the Ce^{4+} state and makes the reduction of CeO_2 unfavorable. In fact, the fluorite structure of ceria is a direct result of the ionic nature of ceria, and of the charge and size of the ions.
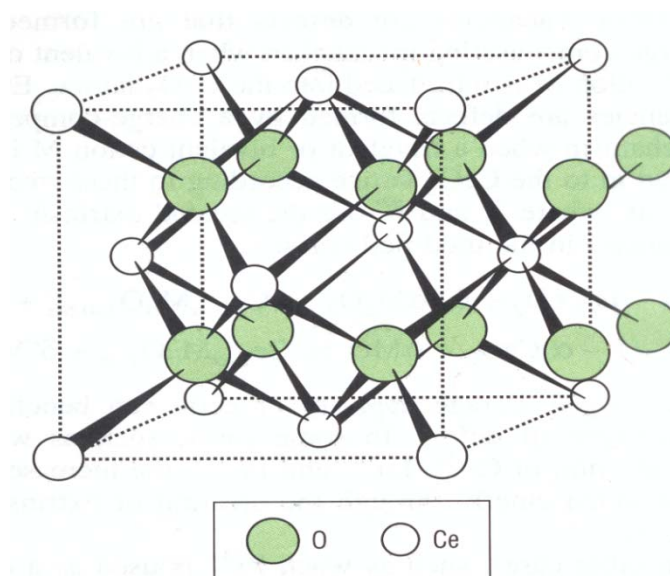
Figure 1.9: Crystal Structure of Ceria [Trovarelli]

Oxygen storage measurements consist in the determination of the amount of a reducing gas (H_2, CO) which is oxidized after passing through an oxygen presaturated catalyst. It deals with the study of a reducer oxidation under transient conditions and in the absence of gaseous oxygen (anaerobic oxidation).Two different measurements of the oxygen storage capacity may be distinguished:

a) The OSC (Oxygen Storage Capacity) is related to the most reactive oxygen species and the most readily available oxygen atoms. OSC may characterize the dynamic of the system.

b) The OSCC (Oxygen Storage Capacity Complete) is the total or maximum oxygen storage capacity. OSCC contains information about the overall reducibility of the solid.

11

The total OSC represents the widest 'limiting' amount of oxygen transferable from the catalyst at a given temperature and generally is limited in the case of CeO_2 by the formation of some non-stoichiometric CeO_{2-x} compounds. The capability of CeO_2-based materials to provide/abstract oxygen at the catalytic site is perhaps a better description of this OSC functionality, where spillover properties, creation and annihilation of oxygen vacancies and complex network of reaction/interactions play a vital role. Oxygen diffusion in ceria and related systems is of interest for several reduction and oxidation reactions.

The incorporation of zirconium into the CeO_2 lattice greatly improves the OSC and promotes oxygen mobility. This specific behavior of mixed oxides is attributed to the participation of bulk oxygen atoms in the storage process (Duprez et al., 1999). The largest OSC is obtained for $Ce_{0.63}Zr_{0.37}O_2$ with 219 µmol O g^{-1} (5.5 µmol O m^{-2}) whose OSC was calculated to be 4 times larger than pure CeO_2
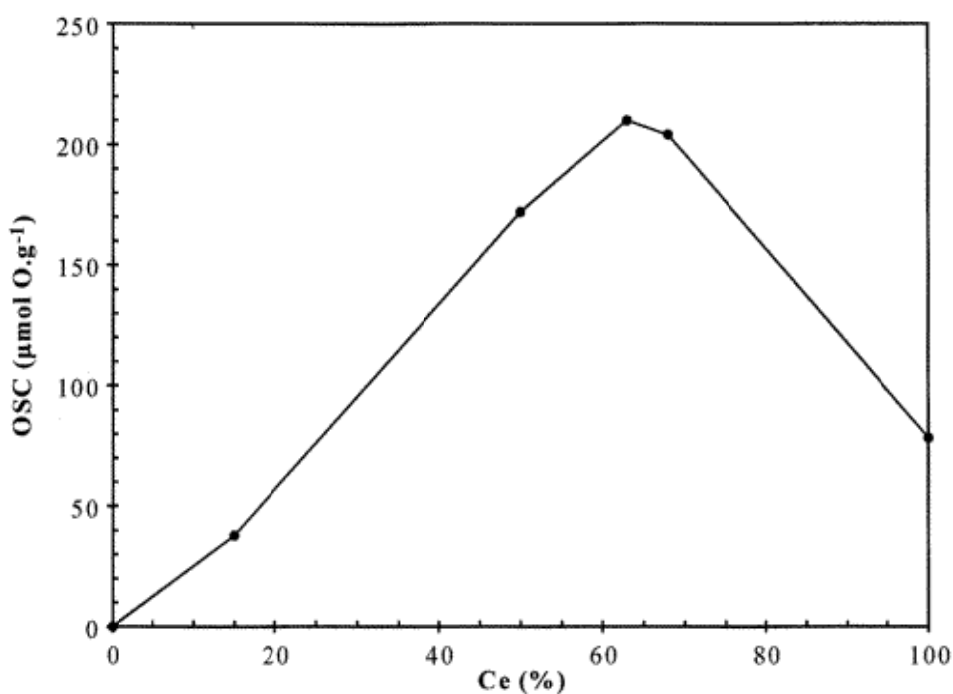
Figure 1.10 Oxygen storage capacity (µmol O g^{-1}) of $Ce_xZr_{(1-x)}O_2$ samples at 400 °C (Maldier et al., 1999)

It was further proposed that the introduction of zirconium induces the formation of structural defects associated with oxygen vacancies. $Ce_{1-x}Zr_xO_2$ solid solutions can exist in three

stable phases (monoclinic (*m*), tetragonal (*t*), cubic (*c*)) and two metastable phases (t', *t*'') under different conditions.

1.4. OBJECTIVES

The primary objective of the present work was to prepare mesoporous ceria, zirconia and their solid solution possessing high surface area, better thermal stability and suitable micro-texture properties. The intensive physicochemical characterizations of the prepared mesoporous metal oxides were done by employing various spectroscopic and non-spectroscopic techniques viz; X-ray diffraction (XRD), BET sorptometry, Thermogravimetry/Differential Thermo Gravimetry (TG-DTA), Scanning Electron Microscopy (SEM), High Resolution Transmission Electron Microscopy (HRTEM) and Fourier Transform Infrared Spectroscopy (FT-IR).

CHAPTER 2

EXPERIMENTAL METHODOLOGY

2.1. STARTING MATERIALS

The chemicals used for preparation are Cerium (III) nitrate hexahydrate (99%) , Zirconium oxy chloride, Zirconium(IV) oxychloride octahydrate (AR grade) and Zirconium(IV) butoxide solution (80 wt. % in 1-butanol) which were obtained from Sigma-Aldrich India Ltd. Ammonium ceric nitrate (99.0 %) were obtained from SD fine chemicals, India. The non-ionic copolymer surfactants such as Triblock copolymer Pluronic P123 (MW=5800, $EO_{20}PO_{70}EO_{20}$) and F127 (MW=12600, $EO_{97}PO6_7EO_{97}$) were purchased from Sigma-Aldrich India Ltd. All other chemicals used in the investigations were of analytical (AR) grade and were obtained from Qualigens, India or S.D. Fine Chemicals, India. These chemicals were used as such without any further purification.

2.2. CHARACTERIZATION TECHNIQUES

In the present investigation a battery of experimental were employed to characterize all the synthesized materials.

2.2.1. X-ray Diffraction (XRD)

X-ray diffraction (XRD) was generally used to investigate the bulk phases present in the sample. X-ray diffraction patterns of various samples were recorded using a Rigaku Miniflex X-ray diffractometer operated at 30 kV using Ni-filtered Cu Kα radiation (λ = 1.5418 Å) in the range of 10-80 degrees at a scan rate of 3 degrees per min. The spacing between two planes d_{hkl} is related to the diffraction angle 2θ by the Bragg law:

$$n\lambda = 2d\ sin\ \theta$$

where,

λ is the wavelength of the X-rays,
d is the distance between two atomic planes in the crystalline phase,
n is the order of the diffraction, and
θ is the incoming diffraction angle.

Identification of phase is generally based on the comparison of the set of reflections of the specimen with that of pure reference phases, or with a database provided by the International Centre for Diffraction Data (ICDD) (formerly ASTM then JCPDS). The powder Xray diffraction (XRD) patterns were recorded on a Rigaku Miniflex II diffractometer .The intensity data were collected over a 2θ range of 2−80°. Diffraction patterns were assigned using the database supplied by the International Centre for Diffraction Data. The crystallite sizes of the materials were calculated by XRD broadening technique employing Debye-Scherrer equation (Cullity, 1971) as shown below:

$$ t = \frac{K\,\lambda}{\beta\,Cos\,\theta} $$

where

    K = constant
    t = crystallite size
    λ = wavelength of the radiation used
    β = integral breadth of peak (full width at half maximum)
    θ = Bragg diffraction angle

2.2.2. BET Surface Area Measurement

The Brunauer-Emmett-Teller (BET) method is a good procedure for measuring surface areas of various materials by physical adsorption of gases. In principle the amount of adsorbate (nitrogen) required to form a monolayer of molecules over the surface of catalyst is given by the following BET equation.

$$ \frac{P}{V_a\,(P_0 - P)} = \frac{1}{V_m\,C} + \frac{C-1}{V_m\,C}\,\frac{P}{P_0} $$

where,

    P is the pressure, P_0 is the saturation vapor pressure,
    V_a is the amount of gas adsorbed at the relative pressure P/P_0,
    V_m is the monolayer capacity, and C is a BET constant.

A plot of $P/V_a\,(P_0-P)$ versus relative pressure of P/P_0 is a straight line with slope of $(C\ 1)/(V_mC)$ and intercept of $1/(V_mC)$, respectively. Knowing slope and intercept permits

15

calculation of Vm. Subsequently the specific surface area of the sample can be determined by the following equation.

$$\text{Specific Surface Area } (m_2 g^{-1}) = \frac{(V_m \ X \ N \ X \ A_m)}{W \ X \ V_o}$$

where,

N is the Avagodro constant ($6.023 \ X \ 10^{23}$ molecules mol^{-1}).

A_m is cross sectional area of adsorbate molecule,

W is the weight of the sample.

V_o is 22414 mL mol^{-1}

In the present investigation, the BET surface areas were determined by N_2 adsorption using a Micromeritics ASAP 2020 instrument. All the samples were out gassed at 400 K for 12 h. High pure nitrogen was used as adsorbate at liquid nitrogen temperature.

2.2.3. Thermal Analysis (TG-DTA)

Thermal analyses of the synthesized samples were carried out on Perkin Elmer TGA (Delta series TGA 7) with a steady heating rate of 10 K/ min. The samples were heated from ambient temperature to 1173 K under air flow at flow rate of 20 mL min^{-1}.Thermal analyses were performed to understand the nature of interaction of the surfactant with the inorganic precursor and to know the calcination temperatures. When a substance is subjected to a programmed heating and cooling, it normally undergoes physical and chemical changes. The gain or loss in weight of a sample as a function of temperature is measured by thermogravimetry (TG).

2.2.4. Scanning Electron Microscopy (SEM)

A finely focused electron beam scanned across the surface of the sample generates secondary electrons, backscattered electrons, and characteristic X-rays. These signals are collected by detectors to form images of the sample displayed on a cathode ray tube screen. Features seen in the SEM image may then be immediately analyzed for elemental composition using Energy Dispersive X-Ray Analysis (EDAX). Secondary Electron Imaging shows the topography of surface features a few nm across. Backscattered Electron Imaging shows the spatial distribution of elements or compounds within the top micron of the sample to study the specific morphology and to assess the elemental composition, SEM analyses were carried out

with Quanta 200 FEG scanning electron microscope operating with an accelerating voltage of 30 kV.

2.2.5. Transmission Electron Microscopy (TEM).

TEM offers the unique advantage of allowing the direct information about the micro texture of the catalyst and structural information by lattice imaging. The technique of high-resolution electron microscopy (HREM) is performed with axial illumination using an objective aperture, which allows several diffracted beams to be combined with the axial transmitted beam to form the image. From images it is possible to obtain accurate information on the shape and size of particles belonging to active phases, structural information such as symmetry and unit cell parameters of crystallites, crystal orientations, lattice defects can be obtained by electron diffraction and lattice imaging techniques. The critical step in electron microscopy is specimen preparation. The thickness of solid phases should be less than 50-100 nm to allow sufficient transmittance. Thinner the samples better the resolution and better contrast. Specimens should be deposited on 2/3 mm diameter copper grids (100−400 mesh) covered with a thin amorphous carbon film. The easiest way is to ultrasonically disperse a few milligram of the powder in a few milliliter of ethanol, take a drop of the suspension deposit it on a carbon coated grid and let the liquid evaporate. In this study, the electron microscopic investigations were carried on a Philips CM12 transmission electron microscope with Energy Dispersive Spectroscopy (EDS) detector for micro-analysis and at an accelerating voltage of 200 kV.

2.2.6. Fourier-transform infrared spectroscopy (FT-IR)

Fourier-transform Infrared spectroscopy (FT-IR) provides qualitative information about the way adsorbed molecules are bonded to the surfaces. Infrared bands are produced if the vibration causes a change in the dipole moment (or induced dipole moment). Infrared light emitted from a source (e.g. a SiC Globar) is directed into an interferometer, which modulates the light. After the interferometer the light passes through the sample compartment (and also the sample) and is then focused into the detector. The signal measured by the detector is called the interferogram. Fourier transform infrared spectra of various samples reported in this study were recorded on a Bruker FT-IR spectrometer (Tensor 27) at ambient conditions. Sample preparation is done by pressing a KBr pellet.

SYNTHESIS AND CHARACTERIZATION OF MESOPOROUS CERIA

3.1. INTRODUCTION

Cerium oxide is one of the most reactive rare earth metal oxides, which has been extensively studied and employed in various applications including fast ion conductors, oxygen storage capacitors, catalysts, UV blockers, polishing materials, and electrolytes for solid oxide fuel cells (SOFC)(Jasinski et al., 2003). Nanocrytalline CeO_2 materials benefit not only those applications, but they also possess some other unique properties, such as the Raman-allowed modes shifting and broadening, lattice expansion, transition from boundary diffusion to lattice diffusion and a blue shift in ultraviolet absorption spectra. Supported CeO_2 and CeO_2-based mixed oxides are effective catalysts for the oxidation of different hydrocarbons, for the production and purification of H_2 and for the removal of organics from polluted water. Such catalytic prowess of ceria comes from its ability to shift between two oxidation states, Ce(III) and Ce(IV), and the high mobility of bulk oxygen species—properties that allow ceria to behave as an oxygen buffer.

Ceria and ceria-based compounds obtained in nano-porous structured forms are expected to be promising as materials that show interesting properties through shape-specific and/or quantum size effects. In addition, a unimodal mesoporous structure with monodisperse spherical particles would result in very high surface area, thermally stable materials that are more amenable to practical applications in areas such as catalysis. However, the basic requirement for many applications of these materials is the preparation, which is not only reproducible on the nano–scale but also with a high surface area, tailored structure and morphology. Herein a simple method to prepare mesoporous ceria utilizing both nanocasting method and the so-called chemical soft templating approach through co-operative self-assembly mechanism using a nitrate salt precursor is reported.

3.2. EXPERIMENTAL

3.2.1. Preparation of mesoporous ceria using silicahard template

1.0 g of SBA-15 template was dispersed in 6 mL of 0.9 M ethanolic solution of cerium nitrate and stirred for several hours in a 25 mL beaker. The mixture was transferred to a clean flat Petri dish and the solvent was evaporated. For achieving higher loadings, the above dried hybrid powder was calcined at 200 °C for 6 h to decompose the nitrate species, and then the impregnation step was repeated, but the amount of precursor was reduced to 2/3 compared to the first step . The resulting sample was calcined in air at 500 °C for 4 h with a heating ramp of 1 K/min to completely decompose the inorganic precursor. Finally, the silica template was removed using a 2 M NaOH aqueous solution at room temperature for 15 hours.

3.2.2. Preparation of mesoporous Ceria using soft template

In this synthesis, cerium nitrate hexahydrate and sodium hydroxide were milled into fine powder and mixed at ambient temperature along with tri-block copolymer P123.The Ce/OH$^-$ molar ratio is about 0.25. The resulting product was transferred into an autoclave at 433 K for 72 hours to further crystallize. After crystallization, the product was washed with de-ionized water until it was free of Cl$^-$ ions, and then washed with ethanol twice to remove water and surfactant contained in the solid. Finally, the samples were dried at 383 K for overnight and calcined at 623 K for 20 hours

3.3. RESULTS AND DISCUSSION

3.3.1. Characterization of mesoporous CeO$_2$ prepared by hard template.

The low angle XRD patterns of the SBA-15/CeO$_2$ composite and the calcined mesoporous CeO$_2$ is shown in Figure 3.1. The mesostructured long range ordering of the composite was confirmed by low-angle XRD. A single well-resolved diffraction peak corresponding to (100) plane, which are characteristics of a 2D hexagonal (p6mm) structure can be easily visualized.
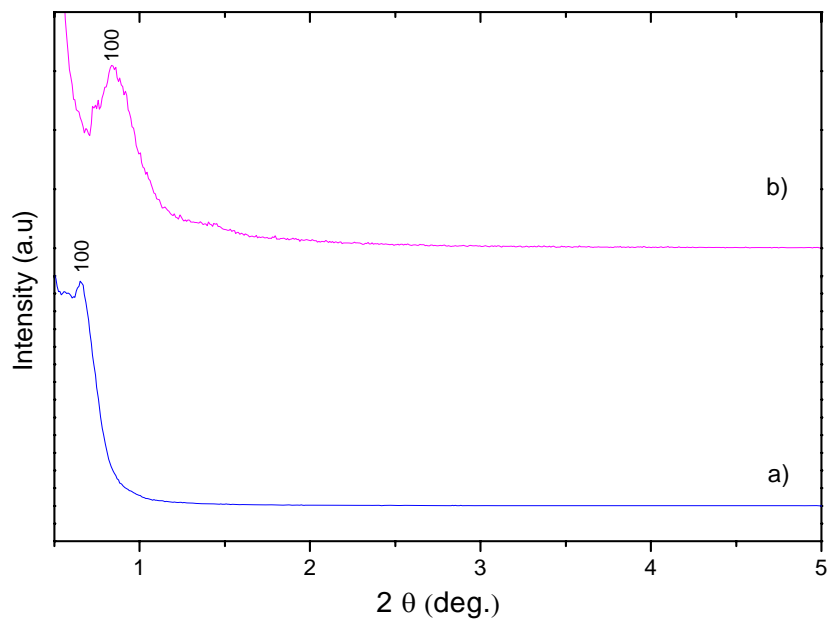
Figure 3.1: Low angle XRD patterns of: (a) CeO_2/SBA-15 and (b) mesoporous CeO_2.

Also Figure 3.2 shows the powder XRD patterns of CeO_2/SBA-15 and that of mesoporous CeO_2 calcined at 773 K. The high-angle XRD patterns of mesoporous CeO_2 is indicative of well-crystallized inorganic frameworks corresponding to the crystalline cubic fluorite ceria phase.
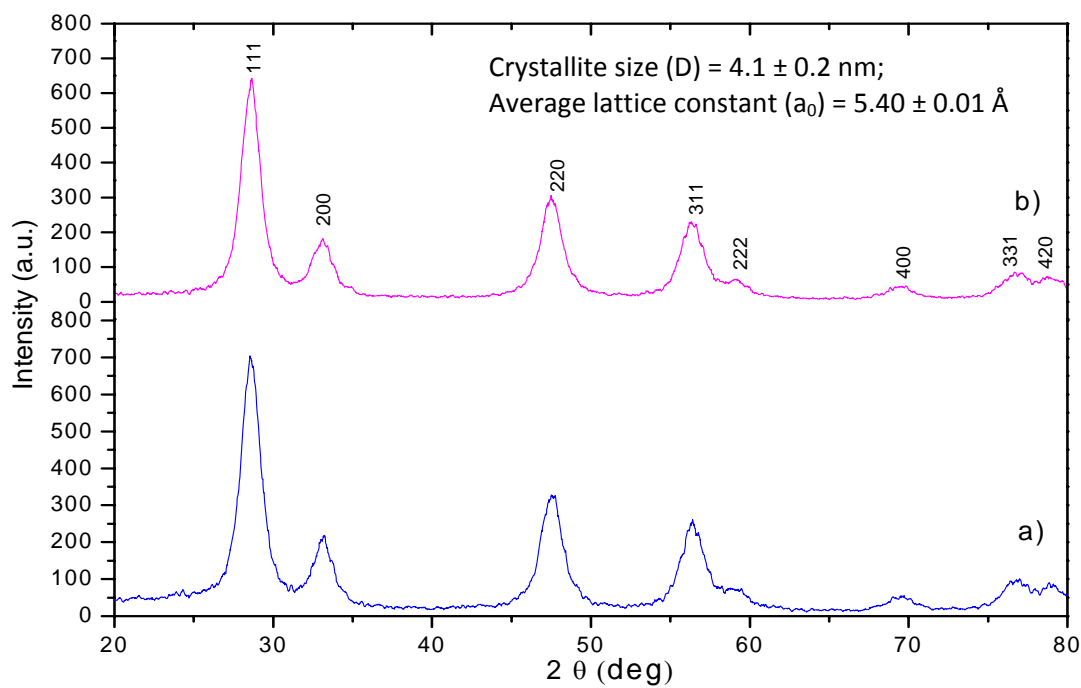
Figure 3.2: XRD patterns of (a) CeO_2/SBA-15, (b) mesoporous CeO_2 calcined at 773 K.

The FT-IR spectra of SBA-15, CeO_2 /SBA-15 and mesoporous CeO_2 are shown in Figure 3.3. Five FT-IR peaks were observed in the spectrum of SBA-15 in the region from 1600 cm^{-1} to 400 cm^{-1}. The bands at 1077 cm^{-1} is attributed to Si–O–Si asymmetric stretching; 946 cm^{-1} to Si–OH stretching; 798 cm^{-1} to Si–O–Si symmetric stretching. The broad band in the 3500–3400 cm^{-1} region (O-H stretching vibration) and a band at 1661 cm^{-1} (O-H bending vibration) indicated the presence of superficial absorbed or crystallized water molecules. The peak at about 1342 cm^{-1} has been found in other CeO_2–SiO_2 systems and is attributed to the presence of Ce–O–Si cross linking. The symmetry stretching and asymmetry stretching bands at 2,915 cm^{-1}, 2835 cm^{-1} of the methyl groups of PEO-block-PPO in the composite is depicted in the Figure 3.3b. The spectra at 712 cm^{-1} can be attributed to the presence of Ce-O bond (Figure 3.3c). When CeO_2/SBA-15 was treated with the NaOH solution, all of the characteristic peaks of SBA-15 disappeared.
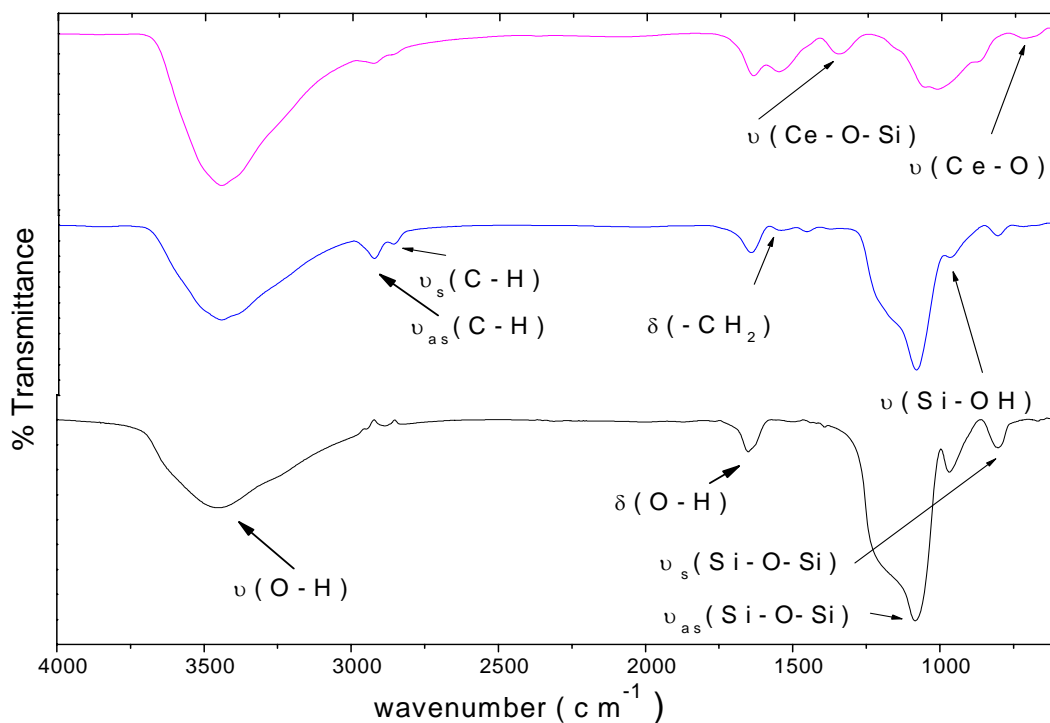
Figure 3.3: FT-IR spectra of (a) SBA-15, (b) ZrO_2 /SBA-15, (c) mesoporous CeO_2.

The N$_2$ physisorption isotherm of the calcined mesoporous CeO$_2$ sample is given in Figure 3.4. The nitrogen sorption isotherms of the rod like CeO$_2$ exhibit a typical type-IV isotherm with a small step and an H1-type hysteretic loop at P/P0 ~0.4–0.8, which is the characteristic of mesoporous metal oxides prepared by hard template route. The uptake at high pressure (P/P0~ 0.8–1.0) for CeO$_2$ is associated with the void spaces between the particles. The presences of regular mesopores are confirmed by the PSD which shows a sharp peak at 3.6 nm as depicted in Figure 3. 4(inset). The specific BET surface area and the total pore volume of the mesoporous ZrO$_2$ product were calculated from the physisorption results to be 143.68m^2/g and 0.289cm^3/g, respectively.
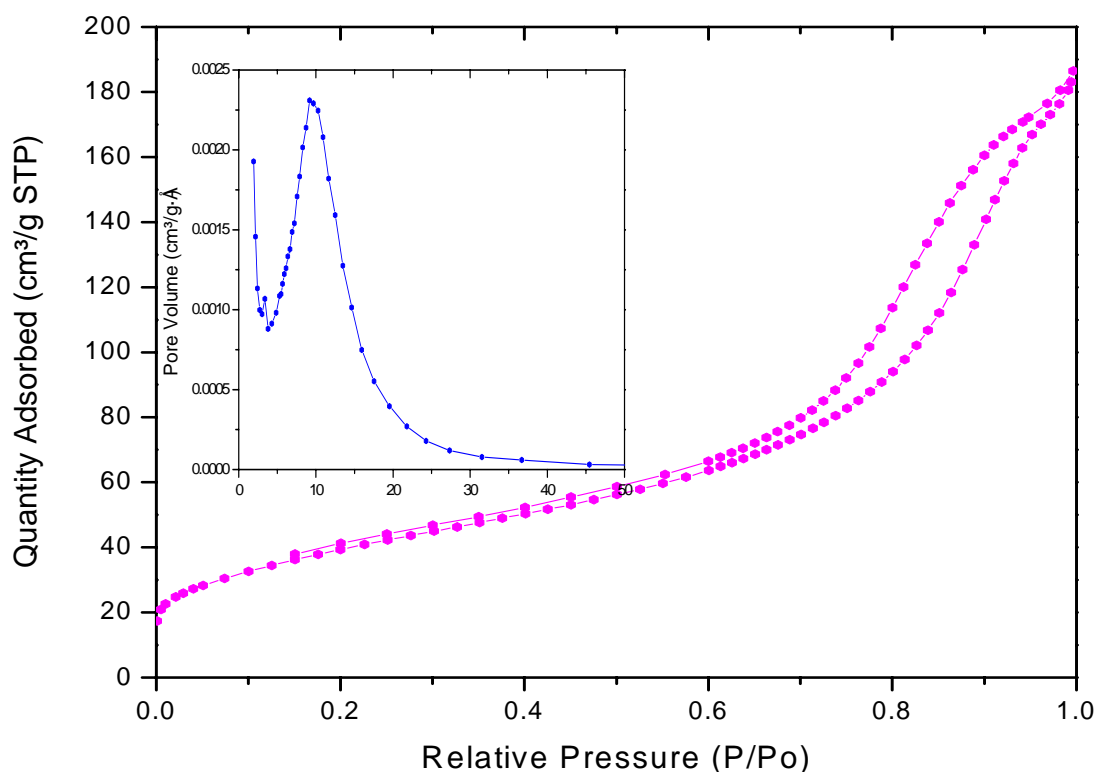
Figure 3.4: N$_2$ sorption isotherms and pore size distribution (insert) of the rod like mesoporous CeO$_2$.

Figure 3.5: Low-(a) and high-magnification (b) SEM images of mesoporous CeO$_2$ rods
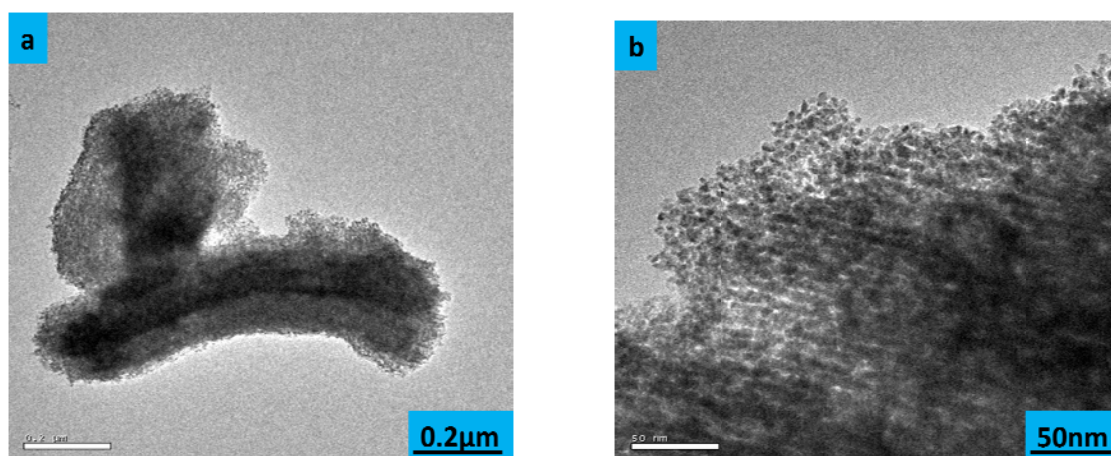
Figure 3.6: TEM images of mesoporous CeO$_2$ rods

Element	Wt %	At %
O K	32.64	68.74
Si K	02.47	03.39
Ce L	64.89	27.87
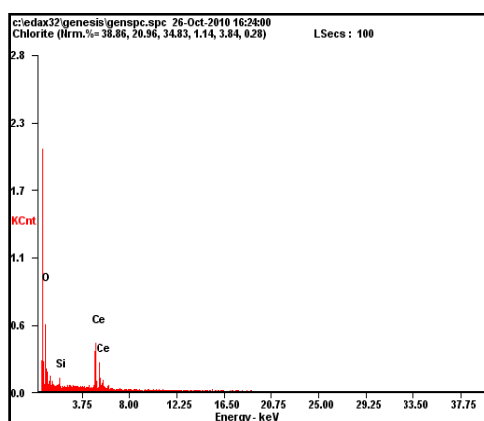
Figure 3.7: EDAX spectrum and elemental quantification of mesoporous CeO$_2$

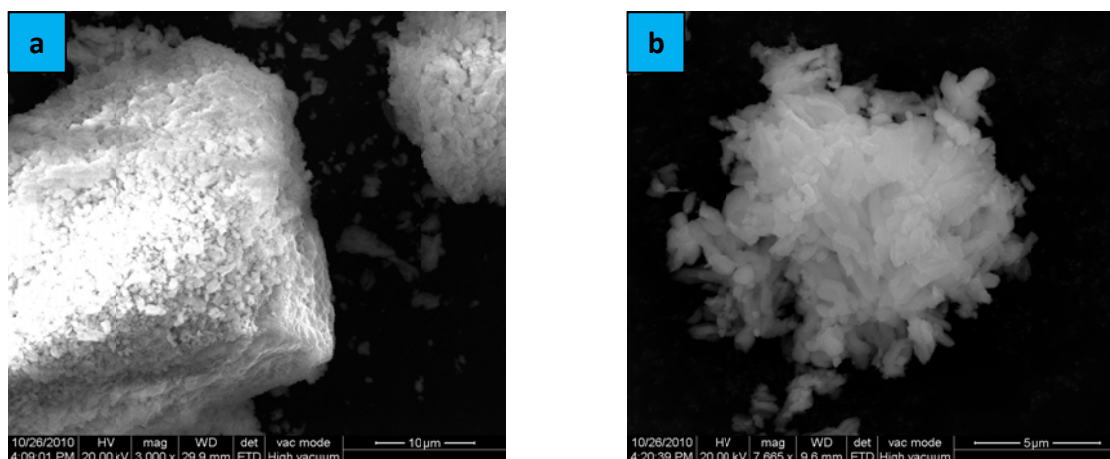The SEM images in Figure 3.5 show that the rod morphology of the SBA-15 templates is replicated in the mesoporous metal oxide. Moreover, EDAX analysis showed that in the mesoporous CeO_2, about 2.47% Si by weight was left in the sample. The TEM images of mesoporous CeO_2 was shown in Figure 3.6. Here pore channel and mesoporous structure with long range order are observed once more. It is thought that the reappearance of the mesopores in the CeO_2 was caused by removal of walls of SBA-15 by reaction with the 2M NaOH solution.

3.3.2. Characterization of mesoporous CeO_2 prepared by soft template

The low angle XRD patterns of the solvent extracted and the calcined mesoporous CeO_2 is shown in Figure 3.8. The mesostructured long range ordering of the composite was confirmed by low-angle XRD. Low-angle XRD pattern exhibits a single well-resolved diffraction peak corresponding to (100) plane, which are characteristics of a 2D hexagonal (*p6mm*) structure.
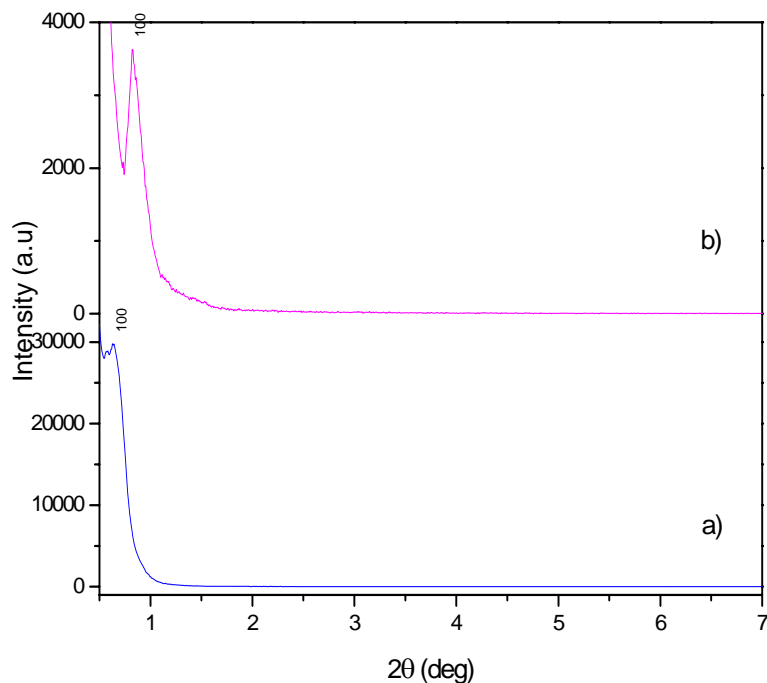
Figure 3.8: Low angle XRD patterns of: a) solvent extracted b) calcined mesoporous CeO_2

Figure 3.9 shows the powder XRD patterns of solvent extracted and that of mesoporous CeO_2 calcined at 623 K. The high-angle XRD patterns of mesoporous CeO_2 is indicative of well-crystallized inorganic frameworks corresponding to the crystalline cubic fluorite ceria phase.

24
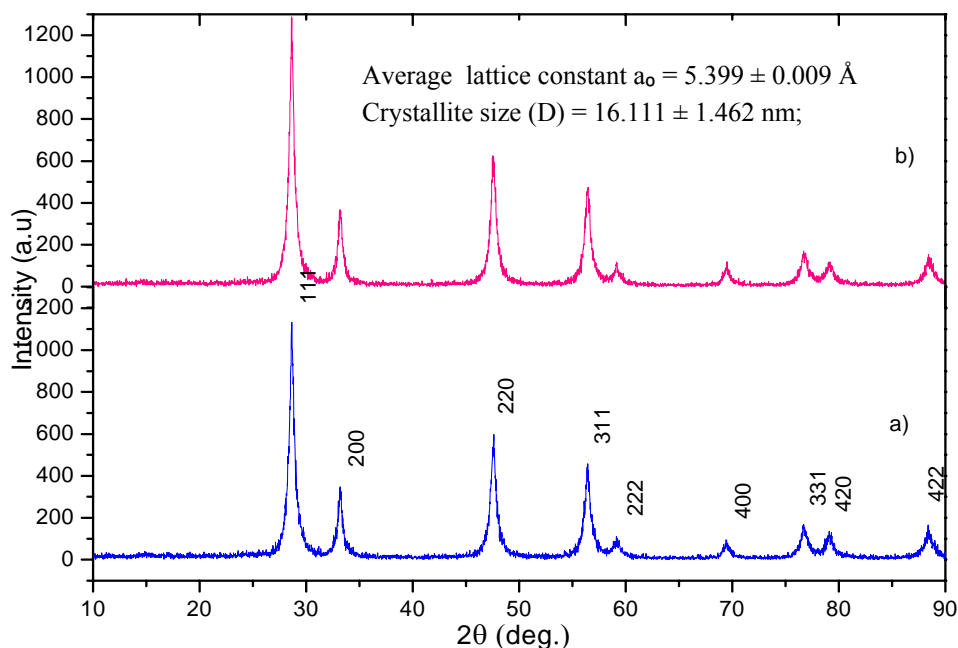
Figure 3.9: XRD patterns of (a) solvent extracted CeO_2, (b) mesoporous CeO_2 calcined at 623K

In the FT-IR spectrum of mesoporous CeO_2 a strong and broad band in the 3500–3400 cm^{-1} region (O-H stretching vibration) and a band at 1630 $cm^{-1}$ (O-H bending vibration) indicated the presence of coordinated water molecules (Figure 3.10 b), with the peak at 1386 cm^{-1} indicating O-H bending vibration. The symmetry stretching and asymmetry stretching bands at 2,920 cm^{-1} and 2,850 cm^{-1} of the methyl groups of PEO-block-PPO in the as synthesized sample is depicted in the Figure 3.10a. The spectra at 750 cm^{-1} can be attributed to the presence of Ce-O bond (Figure 3.10b). However, the peaks arising from the surfactant completely disappear after calcinations.

The N_2 physisorption isotherm of the calcined mesoporous CeO_2 sample is given in Figure 3.11.The nitrogen sorption isotherms of CeO_2 exhibit a typical type-III isotherm with a small step and an H2-type hysteretic loop at P/P0 ~0.6–0.9, which is the characteristic of mesoporous metal oxides prepared by soft template route. The uptake at high pressure (P/P0~ 0.8–1.0) for CeO_2 is associated with the void spaces between the particles. The presences of regular mesopores are confirmed by the PSD which shows a sharp peak at 13.8 nm as depicted in Figure 3.11(inset).

The specific BET surface area and the total pore volume of the mesoporous CeO_2 product were calculated from the physisorption results to be $50.13 m^2/g$ and $0.19 cm^3/g$ respectively
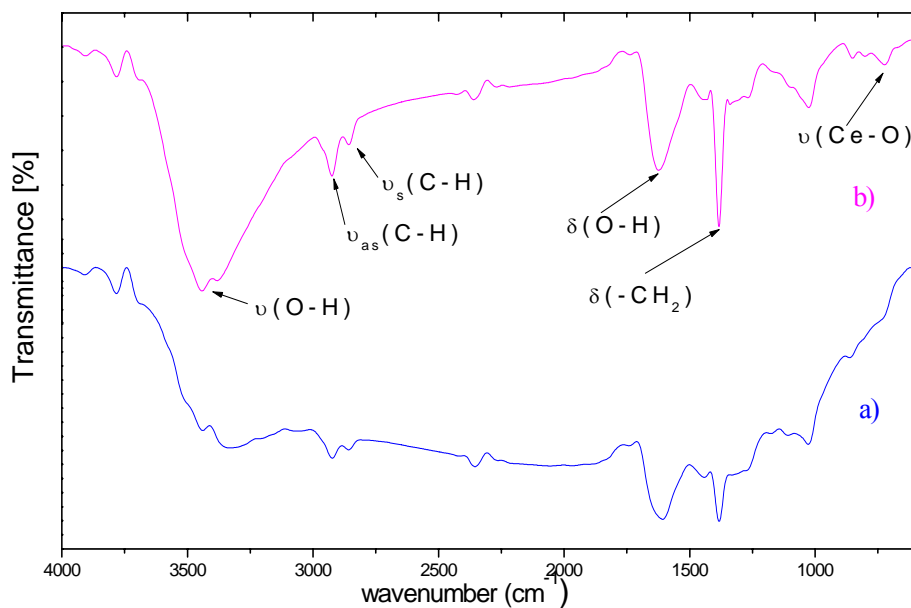
Figure 3.10: The IR spectra of (a) solvent- extracted and (b) calcined CeO_2.
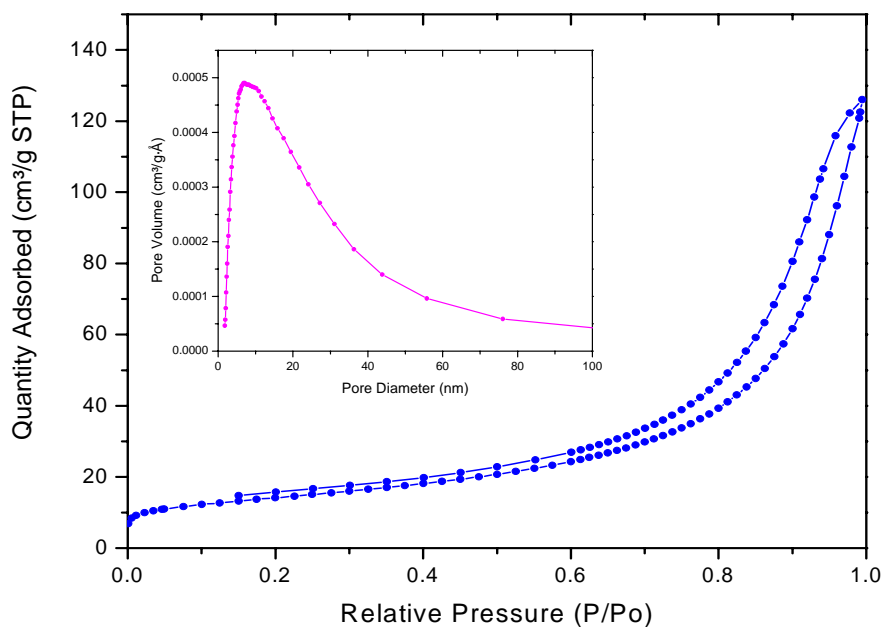
Figure 3.11: N_2 sorption isotherms and pore size distribution (insert) of the mesoporous CeO_2

The SEM images of the solvent extracted and calcined mesoporous CeO_2 shown is Figure 3.12. SEM measurements were performed to assess the external morphologies of the mesoporous

metal oxides. As observed from the SEM images, the samples consist of typical non-homogeneous morphology of nearly unequal particle distribution within the wide size range
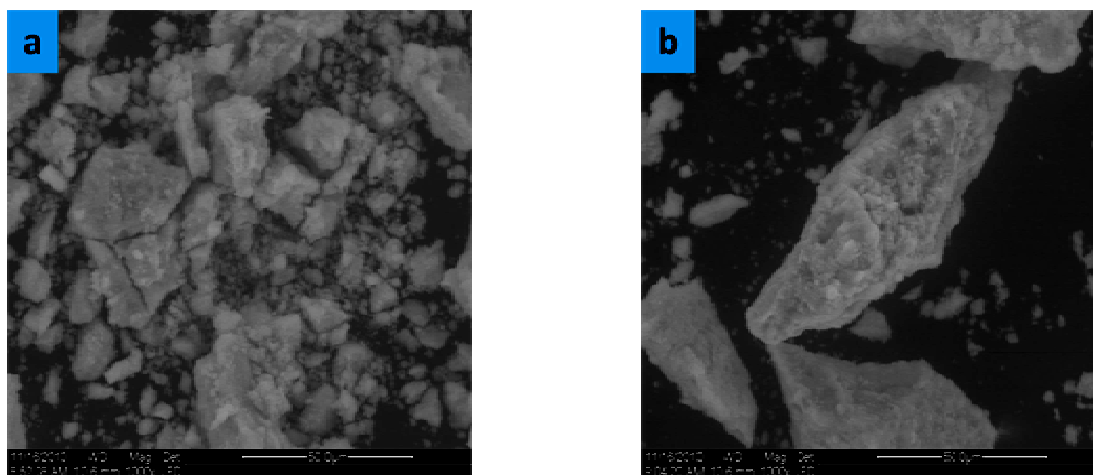
Figure 3.12: SEM images of: a) solvent-extracted and b) calcined mesoporous CeO_2

Table 3.1: Synopsis of Textural Properties of Mesoporous Ceria.

Mesoporous Sample	Template used	BET surface area (m²/g)	Pore volume (cm³/g)	Avg. Pore size (Å)
CeO_2	SBA-15	143.68	8.8	0.29
CeO_2	P123	50.12	13.8	0.19

3.4. CONCLUSION

In conclusion, mesoporous CeO_2 rods possessing high surface area and uniform mesopores can be successfully prepared using simple nanocasting method. The prepared metal oxide is the reverse replica of the hard template and has long range order with hexagonal symmetry, which was further confirmed by the TEM images. Template removal process (NaOH leaching) had been optimized in case of replica method for tuning the textural and morphological features of the mesoporous ceria.But mesoporous silica is not the appropriate hard template because Si cannot be removed completely from the product For retaining mesostucture in case of co-operative self-assembly process, the ethanol extraction technique which is an optimum method for removing non ionic surfactant was utilized. Furthermore mesoporous ceria having good microtexture properties cannot be prepared through the so called chemical soft templating. This simple nanocasting method can be used to synthesis other morphology controllable mesoporous metal oxides and sulfide.

CHAPTER 4

SYNTHESIS AND CHARACTERIZATION OF
MESOPOROUS ZIRCONIA

4.1. INTRODUCTION

Mesoporous materials have attracted widespread interest in different areas of science because of their unparallel properties like high surface area, uniform pore size distribution, and large pore volume since the first report of M41S materials. Their convenient synthesis through different chemical routes, their large variety of framework structures and their novel properties have made these materials, a very active area of research as they find applications in many frontier areas such as catalysis, adsorption, biomolecular separation, drug delivery and so on. Among the widely studied transition metal oxides, zirconia is of particular interest because it possesses acidic surface active sites, excellent ion-exchange capacity and rich surface oxygen defects, which provide multi-functionalities common in catalysis electron charge transfers processes. A number of synthesis strategies have been proposed for the synthesis of zirconia mesostructure such as supramolecular self-assembly via electronic, covalent bonding, hydrogen bonding, scaffold mechanism and nanocoating using siliceous mesoporous framework as hard templates. The unique feature for the synthesis of mesoporous materials is focused on the use of supramolecular assembly of template molecules as structure-directing agent in nonaqueous solution via the S^0I^0 templating mechanism (Yang et al., 1999). The soft templates such as triblock copolymers or neutral surfactants, which form the self-aggregated superstructures in solution phase, play the key role in directing the formation of organized porous structures. The mesoporous zirconia can be synthesized using hard template SBA-15 and block copolymer surfactant P123 as structure directing agent. Moderately ordered mesostructure can be achieved at high Zr/OH^- molar ratio. Even the surface area and pore structure of zirconia can be tailored using simple synthesis parameters such as Zr/OH^- molar ratio and crystallization temperature and time. Moreover, prepared mesoporous zirconia possesses high thermal stability (Liu et al., 2008).

4.2. EXPERIMENTAL

4.2.1. Preparation of mesoporous Zirconia using soft template P123 as surfactant.

In this synthesis, zirconyl chloride and sodium hydroxide were milled in to fine powder and mixed at ambient temperature along with triblock copolymer P123.The Zr/OH⁻ molar ratio for two samples were 0.5 and 0.6 respectively. The resulting product for the sample having lower Zr/OH⁻ molar ratio was transferred into an autoclave at 423 K for 48 hours to further crystallize. The crystallizing time and temperature was increased by 24 hours and 50 K respectively for the sample with higher Zr/OH⁻molar ratio. After crystallization, the product was washed with deionized water until it was free of Cl⁻ ions, and then washed with ethanol twice to remove water and surfactant contained in the solid. Finally, the samples were dried at 383 K for overnight and calcined at 623 K for 20 hours.

4.2.2. Preparation of mesoporous Zirconia using SBA-15 silicate as hard template.

1.0 g of SBA-15 was added to 6.0 g of a clear aqueous solution containing 1.8 g of $ZrOCl_2$. 8 H_2O, and the mixture was kneaded three times. After drying at 373 K, the $ZrOCl_2$/SBA-15 obtained was calcined from room temperature to 873 K with a ramp rate of 1 K min⁻¹ and maintained at 873 K for 5 h in order to decompose the inorganic salts completely, thus forming ZrO_2/SBA-15. To remove the silica template, the ZrO_2/SBA-15 was reacted with 2M aqueous NaOH solution for 12 h and washed with deionised water at least three times. The resultant solid was centrifuged and washed with deionised water, washed with ethanol and dried at 373 K to obtain the mesoporous ZrO_2.

4.3. RESULTS AND DISCUSSION

4.3.1. Characterization of mesoporous ZrO_2 prepared by soft template.

The low angle XRD patterns of the as-synthesized and the calcined mesoporous ZrO_2 prepared at Zr/OH⁻ molar ratio of 0.5 and 0.6 is shown in Figure 4.1 and Figure 4.2 respectively. Two peaks are observed in the calcined sample synthesized with Zr/OH⁻ molar ratio of 0.5, while only a primary diffraction line is seen in the sample for Zr/OH⁻ molar ratio of 0.6.

Figure 4.1: Low angle XRD patterns of (a) as-synthesized and (b) calcined ZrO_2 prepared with Zr/OH^- molar ratio of 0.5

Figure 4.2: Low angle XRD patterns of (a) as-synthesized and (b) calcined ZrO_2 prepared with Zr/OH^- molar ratio of 0.6

The wide angle XRD patterns of the as-synthesized and the calcined mesoporous ZrO_2 prepared at different Zr/OH^- molar ratio is shown in Figure 4.3 and 4.4 respectively. The wide-angle peaks shown in Figure 4.3b indicate that the inorganic framework of calcined sample prepared at low Zr/OH^- molar ratio consists mainly tetragonal phase but a very small amount of monoclinic ZrO_2 seems to have been present because of the appearance of an indistinct peak at $2\theta \sim 28.1°$, corresponding to the ($\bar{1}11$) plane, which is the strongest diffraction peak for monoclinic ZrO_2. Exclusive monoclinic phase of zirconia is retained in the calcined samples prepared at high Zr/OH^- molar ratio.
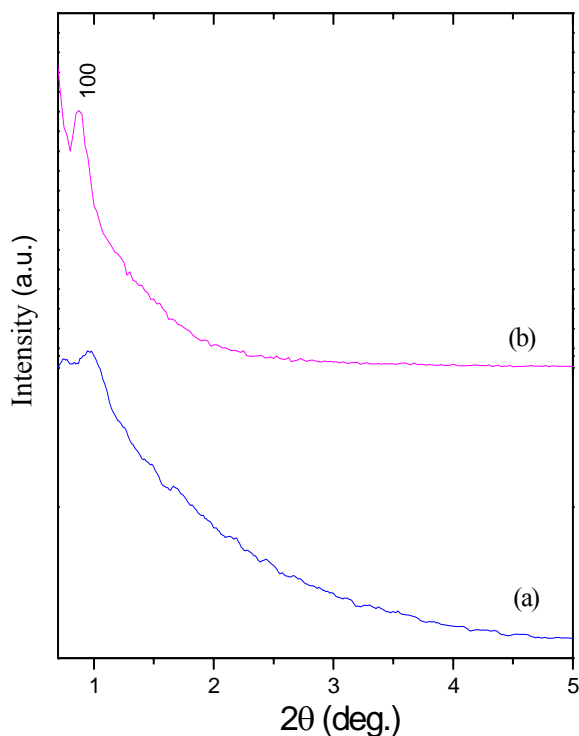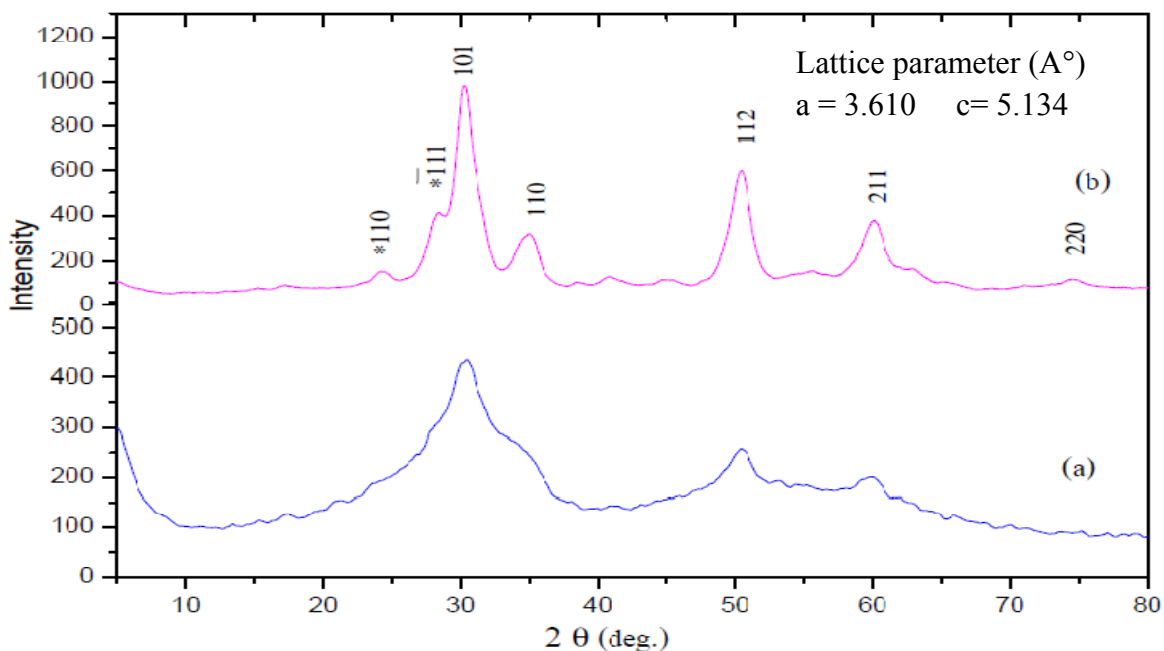
Figure 4.3: XRD patterns of (a) as-synthesized and (b) calcined ZrO_2 prepared with Zr/OH^- molar ratio of 0.50. Planes corresponding to monoclinic phases are indicated by (*)
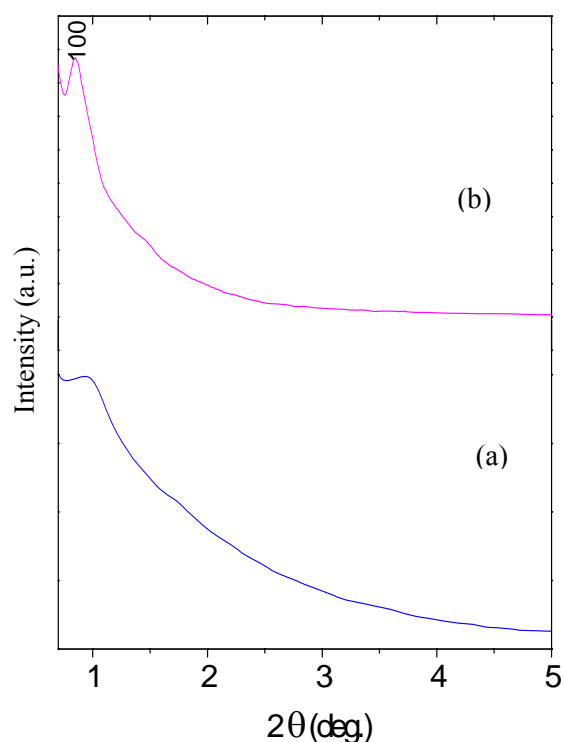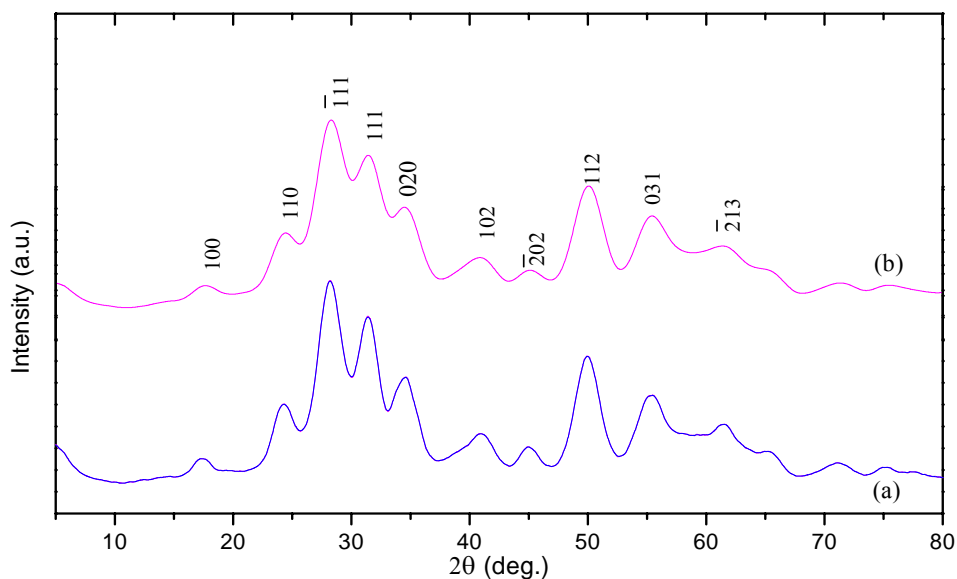

Figure 4.4: XRD patterns of: (a) as-synthesized and (b) calcined ZrO_2 prepared with Zr/OH^- molar ratio of 0.6

In the FT-IR spectrum of mesoporous ZrO_2 a strong and broad band in the 3500–3400 cm^{-1} region (O-H stretching vibration) and a band at 1630 cm^{-1} (O-H bending vibration) indicated the presence of coordinated water molecules (Figure 4.5a).The symmetry stretching and asymmetry

32

stretching bands at 2,920 cm^{-1} 2,850 cm^{-1} of the methyl groups of PEO-block-PPO in the as synthesized sample is depicted in the Figure 4.5a. The spectra at 750 cm^{-1} can be attributed to the presence of Zr-O bond (Figure 4.6a). However, the peaks arising from the surfactant completely disappear after calcinations.

Figure 4.5: IR spectra of (a) as-synthesized; (b) calcined ZrO_2 prepared with Zr/OH$^-$ = 0.5 (molar ratio).
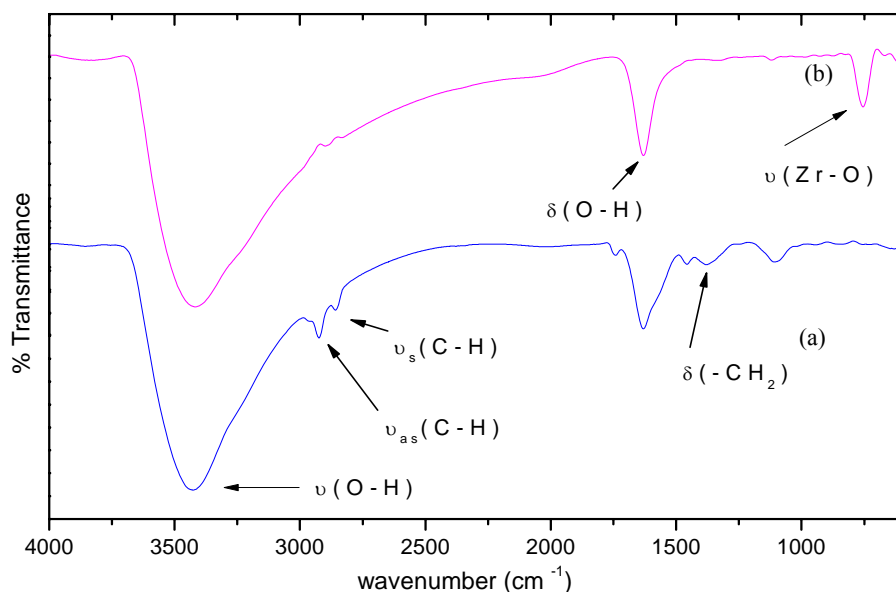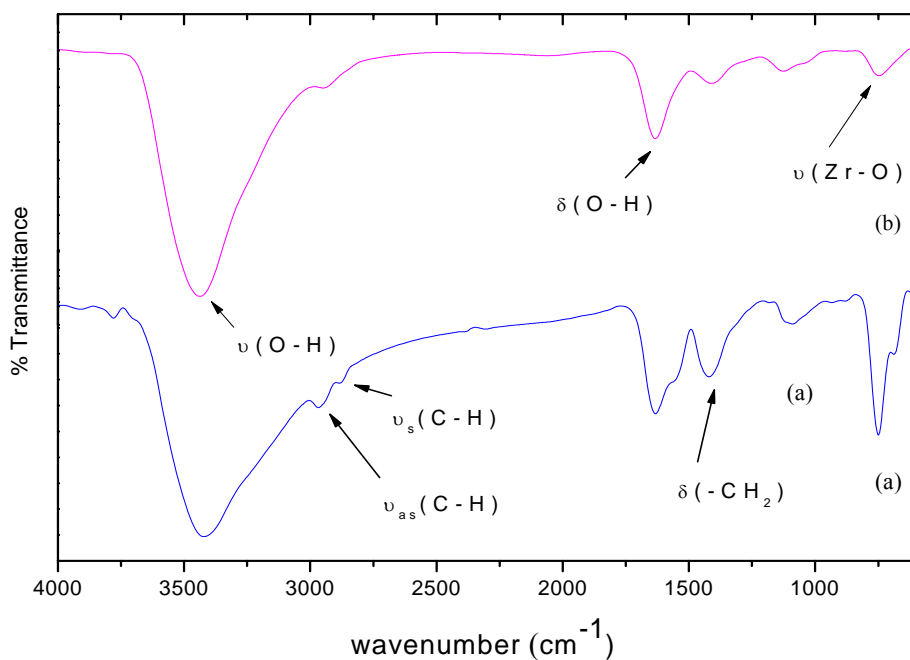

Figure 4.6: IR spectra of (a) as-synthesized; (b) calcined ZrO_2 prepared with Zr/OH$^-$ = 0.5 (molar ratio).

The preparation parameters have strong influence on the mesostructure of zirconia prepared by this solid-state reaction method. It should be noted that Zr/OH⁻ molar ratio exerted a strong effect and is the most important parameter as it controls the mesophase structure and pore size as well. The pore size increases with increasing Zr/OH⁻ molar ratio from 0.5 to 0.6 as evident from Figure 4.8. Moreover Figure 4.7 shows nitrogen sorption isotherms that are characteristic of mesoporous materials. The presences of regular mesopores are confirmed by the PSD which shows a peak maximum around 5.5 nm and 15.5 nm for samples prepared at Zr/OH⁻ molar ratio of 0.5 and 0.6 respectively as depicted in Figure 4.8. The specific BET surface area and the total pore volume of the mesoporous ZrO_2 prepared at Zr/OH⁻ molar ratio of 0.5 were calculated from the physisorption results to be 151.4 m^2/g and 0.24 cm^3/g respectively; for the sample having Zr/OH⁻ molar ratio of 0.6 the corresponding values are 165.7 m^2/g and 0.31 cm^3/g respectively.
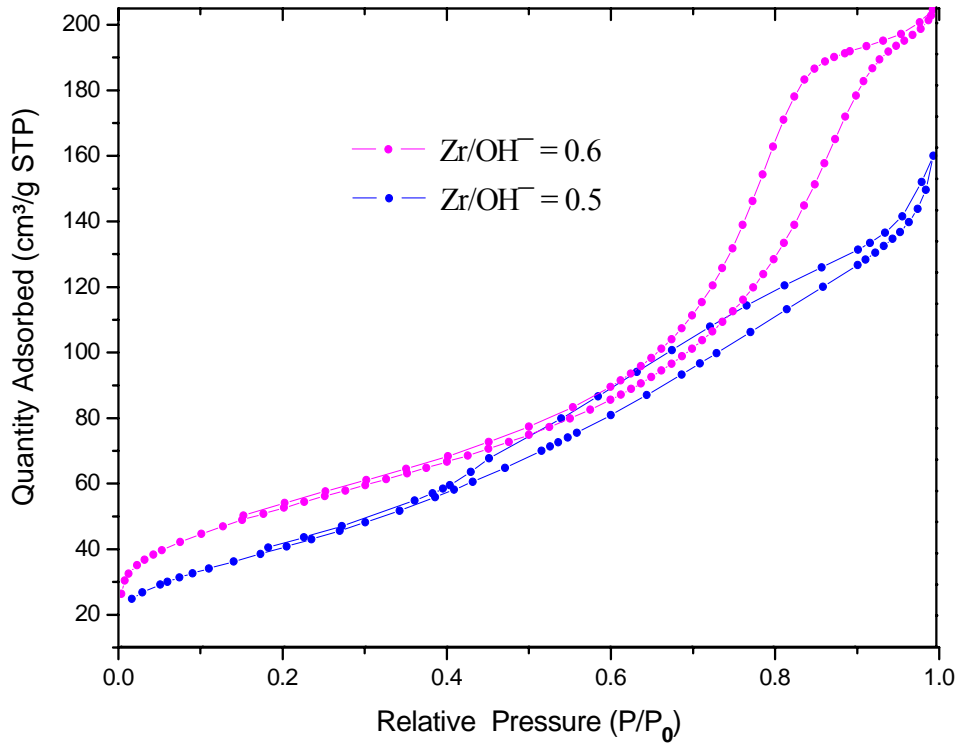
Figure 4.7: Nitrogen adsorption desorption isotherms for mesoporous ZrO_2 prepared at different Zr/OH⁻ molar ratio.
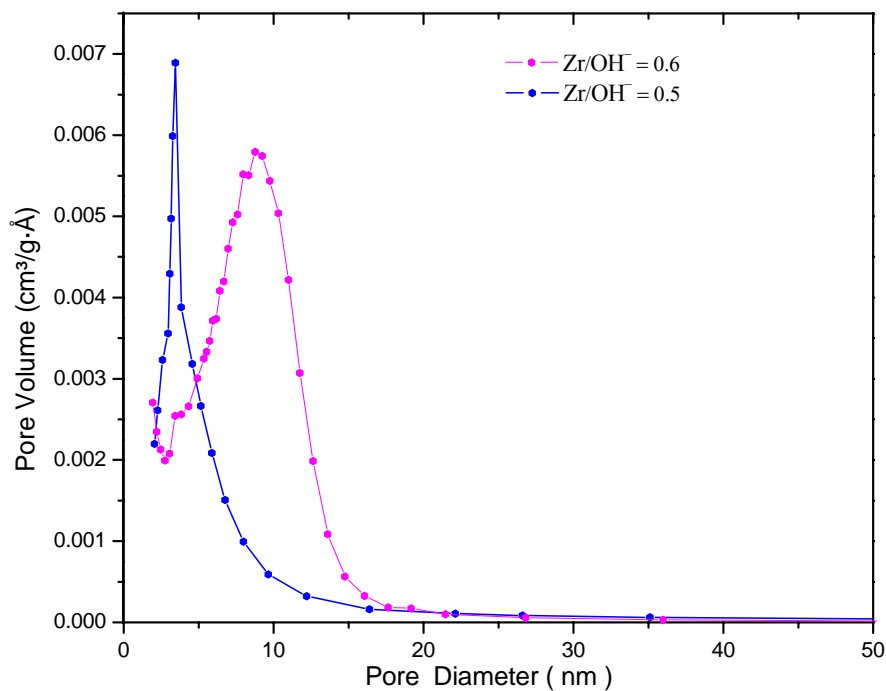
Figure 4.8: Pore size distribution calculated from the desorption branch using the BJH method for mesoporous ZrO_2 prepared at different Zr/OH^- molar ratio.
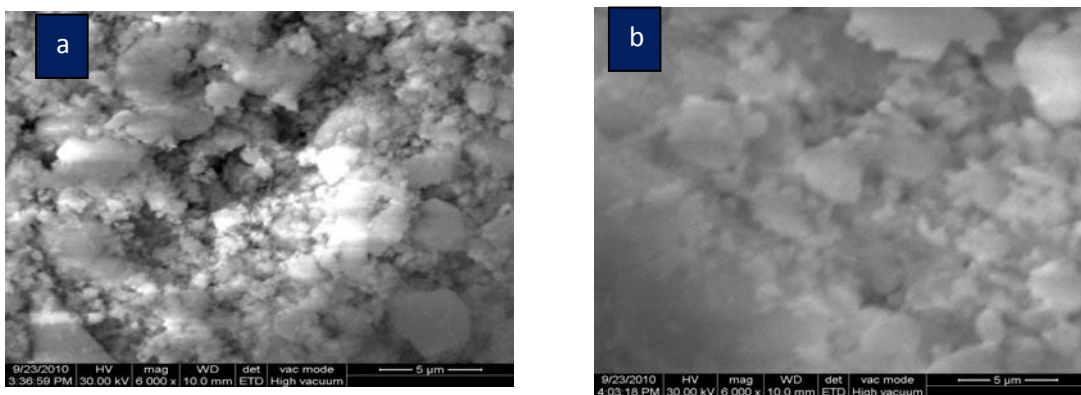
Figure 4.9: SEM images of zirconia prepared at (a) Zr/OH^- =0.5 and (b) Zr/OH^- =0.6 molar ratios.

SEM images as shown in Figures 4.9 demonstrate that the mesoporous zirconia prepared at different Zr/OH^- molar ratios exhibit typical mesostructures. The sample prepared at low Zr/OH^- molar ratio show less ordered structure. In contrast, samples prepared at high Zr/OH^- molar ratio display ordered structure that is similar to the wormhole-like mesostructure.

4.3.2. Characterization of mesoporous ZrO$_2$ prepared by hard template.

The low angle XRD patterns of the SBA-15/ZrO$_2$ and the calcined mesoporous ZrO$_2$ is shown in Figure 4.10. Three well resolved peaks corresponding to (100), (110) and (200) planes attributed to 2D hexagonal (p6mm) symmetry can be visualized in the composite. Figure 4.11 shows the powder XRD patterns of ZrO$_2$/SBA-15 composite calcined at 873 K and that of mesoporous ZrO$_2$. The higher angle XRD patterns of mesoporous ZrO$_2$ shown in Figure 4.11 is indicative of well-crystallized inorganic frameworks corresponding to tetragonal phase.
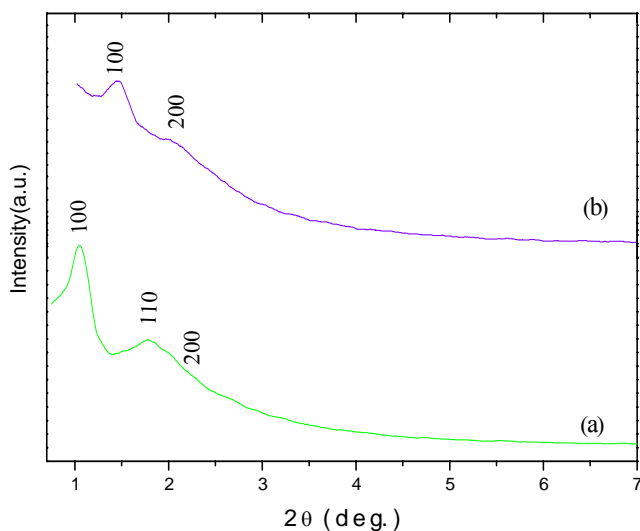
Figure 4.10: Small angle XRD patterns of: (a) ZrO$_2$/SBA-15 and (b) mesoporous ZrO$_2$.
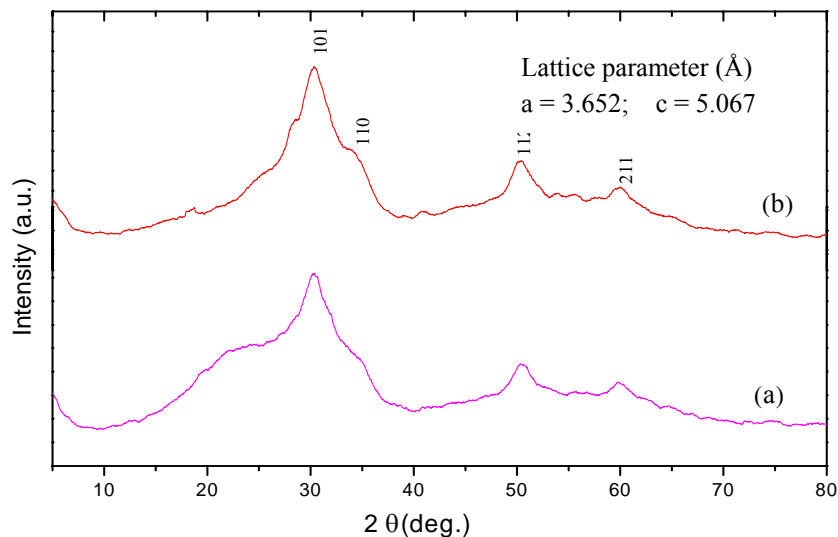
Figure 4.11: XRD patterns of ZrO$_2$/SBA-15 calcined at (a) 873 K, (b) mesoporous ZrO$_2$.

The FT-IR spectra of SBA-15, ZrO_2/SBA-15 and mesoporous ZrO_2 are shown in Figure 4.12. Four FT-IR peaks were observed in the spectrum of SBA-15 in the region from 1600 cm^{-1} to 400 cm^{-1}. The bands at 1080 cm^{-1} are attributed to Si–O–Si asymmetric stretching; 945 cm^{-1} to Si–OH stretching; 796 cm^{-1} to Si–O–Si symmetric stretching. The peak at about 1000 cm^{-1} has been found in other ZrO_2–SiO_2 systems and is attributed to the presence of Zr–O–Si cross linking. When ZrO_2/SBA-15 was treated with the NaOH solution, all of the characteristic peaks of SBA-15 disappeared as shown in Figure 3(d).
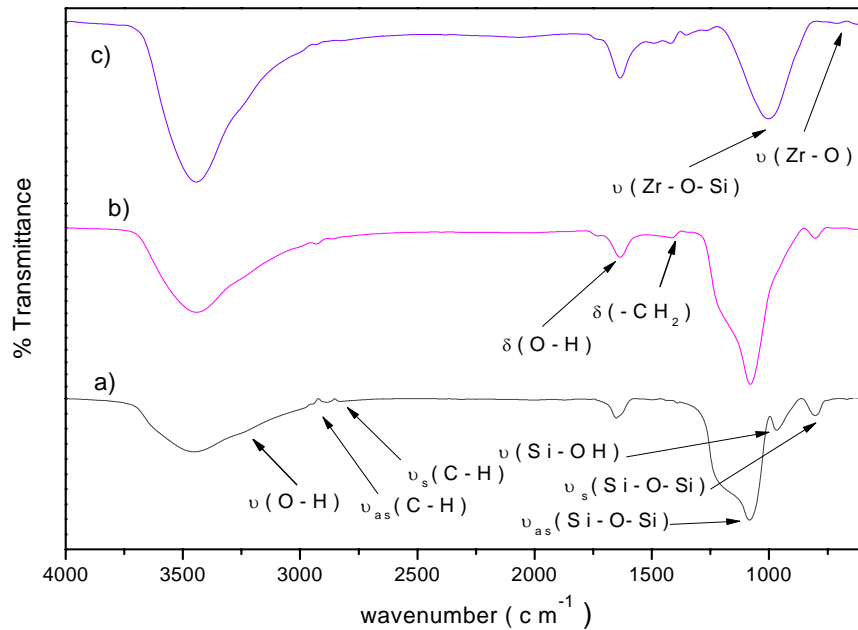
Figure 4.12: FT-IR spectra of (a) SBA-15, (b) ZrO_2/SBA-15 and (d) mesoporous ZrO_2

The N_2 physisorption isotherm of the mesoporous ZrO_2 sample is given in Figure 4.13. A gradual increase in slope started at a relative pressure of ca. 0.4, and was followed by a sharp increase from relative pressure of ca. 0.8 up to ca. 1.0 in both the adsorption and the desorption branches. The more gentle upward slope from ca. 0.4 also corresponds to capillary condensation, typical of mesoporous materials with uniform pore systems, while the further increase at higher relative pressures indicates substantial interparticle porosity. The presences of regular mesopores are confirmed by the PSD which shows a sharp peak at 3.6 nm as depicted in Figure 4.13. The

specific BET surface area and the total pore volume of the mesoporous ZrO_2 product were calculated from the physisorption results to be 216.5697 m^2/g and 0.17 cm^3/g, respectively.
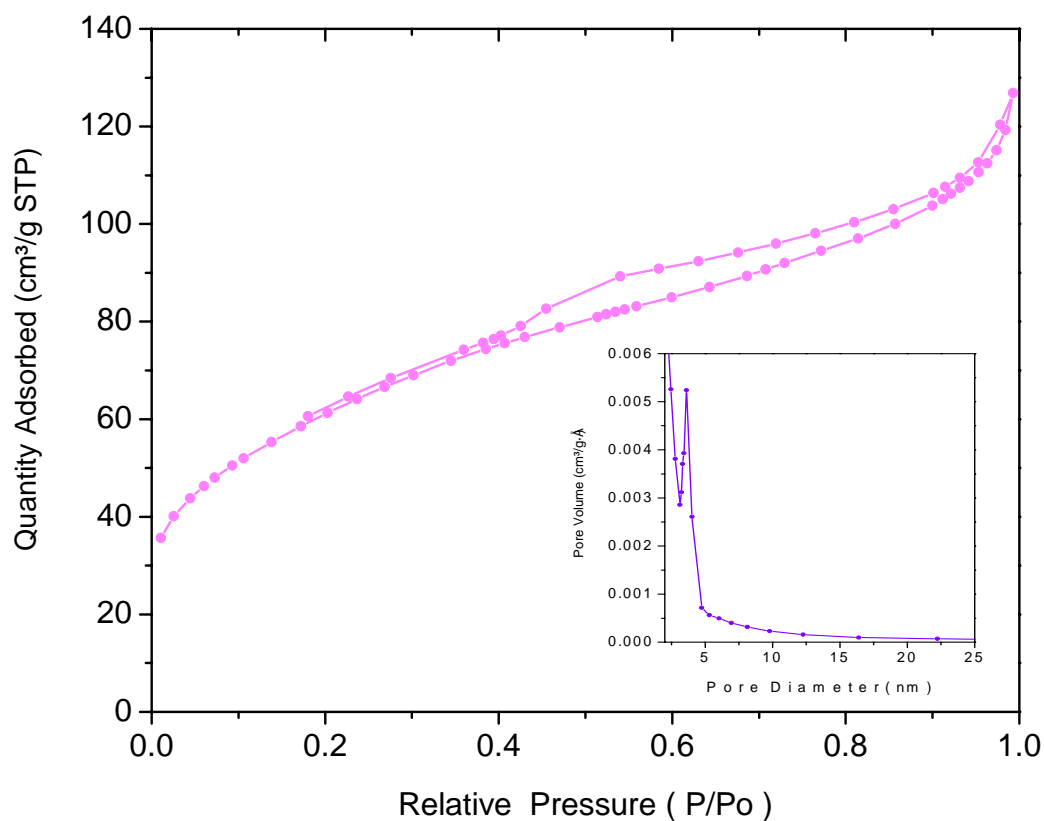
Figure 4.13: N_2 sorption isotherms and pore size distribution (insert) of the mesoporous ZrO_2.

Table 4.1: Synopsis of Textural Properties of Mesoporous Zirconia.

Mesoporous Sample	Template used	BET surface area (m²/g)	Pore volume (cm³/g)	Avg. Pore size (Å)
ZrO_2 (Zr /OH⁻= 0.5)	P123	151.4	5.5	0.24
ZrO_2 (Zr /OH⁻ = 0.6)	P123	165.7	15.5	0.31
ZrO_2	SBA-15	216	3.6	0.17

4.4 CONCLUSION

In summary, the mesoporous ZrO_2 prepared via the replica method with SBA-15 as the hard template had the same rope-like domains and p6mm symmetry as the parent SBA-15. The silica walls were successfully removed after reacting with NaOH solution. Some residual silicon remained in the mesoporous ZrO_2. It was found that this was because of the formation of Zr–O–Si crosslinks, rather than retention of bulk silica or formation of zirconium silicate. These crosslinks were found to stabilise the tetragonal phase of ZrO_2. Although replica method itself was successfully applied to prepare ordered mesoporous ZrO_2, but that mesoporous silica is not the appropriate hard template because Si cannot be removed completely from the product.

Mesostructured zirconia could also be prepared via cooperative self assembly mechanism of the so called chemical soft templating method combined with block-copolymer P123 as structure-directing agent. However the crystal phase transformation from tetragonal to more thermodynamically favorable monoclinic phase was observer at higher Zr/OH^- molar ratio. Using this novel method, the surface area and the pore structure can be tailored by controlling the synthesis parameters such as Zr/OH^- molar ratio and crystallization time and temperature. This novel method is potentially useful to forming mesostructures of many other metal oxides.

CHAPTER 5

SYNTHESIS AND CHARACTERIZATION OF
MESOPOROUS CERIA-ZIRCONIA SOLID SOLUTION

5.1. INTRODUCTION

Great interest has been focused on the mesoporous metal oxides due to their potential application in various areas. Recently, ceria-based materials are of intensive interest because they are commercially employed as the components of ultraviolet radiation absorbers, automotive threeway catalysts (TWCs), solid oxide fuel cells, and glass-polishing materials, and so forth. As a very important material for exhaust catalysis, ceria–zirconia solid solutions are known to work effectively benefitting the advantage of large oxygen storage-release capacity of ceria thanks to its the reversible reaction of Ce^{4+} to Ce^{3+}. Ceria, however, lacks high temperature stability, a problem which is solved through adding zirconia to ceria lattice. Incorporation of zirconium, also, reduces the electrical resistivity of the material making it more adequate for oxygen sensing. Recent studies show that zirconia–ceria solid solution exhibits high thermal stability and excellent oxygen storage capacity, the latter is particularly interesting for NO reduction in the fuel-lean combustion because it makes possible storing the excess oxygen into the bulk of the catalysts in the oxygen-rich condition and to obtain the highest efficiency for pollution abatement . Ceria-zirconia is currently regarded as a potential material used as support or main component in the washcoat in the TWCs (Brezesinski et al., 2005).

Here a novel direct and reproducible method for preparing a highly ordered mesoporous $Ce_{1-x}Zr_xO_2$ solid solution with a 2D hexagonal mesostructure is reported. The general synthesis strategy is based on a liquid crystal templating approach combined with evaporation-induced self-assembly (EISA) in ethanol using block copolymer Pluronic P123 as the template and ceric nitrate and zirconium oxide chloride as the precursors without additional acid or base. These materials, fabricated by the evaporation-induced self-assembly (EISA) process, have shown improved physicochemical properties and thermal stability, so that they could be employed directly for the purpose of the multi- functional oxides. (Brezesinski et al., 2006).

5.2. EXPERIMENTAL SECTION

5.2.1. Preparation of mesoporous $Ce_{1-x}Zr_xO_2$ using EISA method.

In a typical synthesis 1g of Pluronic P123 (M_{av} = 5800, $EO_{20}PO_{70}EO_{20}$) in 20 mL of ethanol. Then quantitative $Ce(NO_3)_3 \cdot 6H_2O$ and $ZrOCl_2 \cdot 8H_2O$ were added (total amount of Ce and Zr is 10 mmol). After stirring for at least 2 h at room temperature, the homogeneous sol was transferred to an oven under desired temperature and humidity (temperature: 40°C, relative humidity: 50%) and underwent solvent evaporation. After 48 h aging, the gel product was dried at 100°C for 24 h. Calcination was carried out by slowly increasing temperature from room temperature to 400°C ($1°C \, min^{-1}$ ramping rate) and heating at 400°C for 4 h in air.

5.3. RESULTS AND DISCUSSION

5.3.1. Characterization of mesoporous $Ce_{1-x}Zr_xO_2$ where x = 0.3 and 0.4.

The low angle XRD patterns of the calcined mesoporous $Ce_{0.6}Zr_{0.4}O_2$ and $Ce_{0.7}Zr_{0.3}O_2$ are shown in Figure5.1a and b respectively. The mesostructured long range ordering of the composite was confirmed by low-angle XRD. Low-angle XRD pattern, shown in Figure 5.1a, exhibits a single well-resolved diffraction peak corresponding to (100) plane, which are characteristics of a 2D hexagonal (*p6mm*) structure.
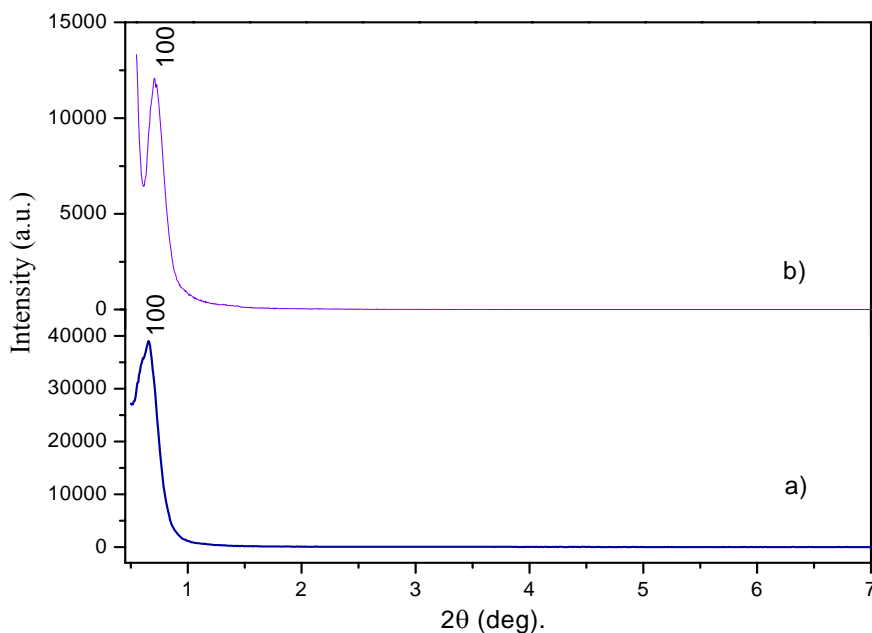

Figure 5.1: SXRD patterns of mesoporous: a) $Ce_{0.7}Zr_{0.3}O_2$ and b) $Ce_{0.6}Zr_{0.4}O_2$

The high-angle XRD patterns of calcined mesoporous $Ce_{0.7}Zr_{0.3}O_2$ and $Ce_{0.6}Zr_{0.4}O_2$ calcined at 673 K is shown in Figures 5.2a and b respectively. The XRD patterns of mesoporous $Ce_{1-x}Zr_xO_2$ is indicative of well-crystallized inorganic frameworks corresponding to the crystalline cubic fluorite phase. According to the Scherrer equation, the crystallite size of calcined samples are 5.8 ± 0.8 nm and 4.7 ± 0.8 nm for mesoporous $Ce_{0.7}Zr_{0.3}O_2$ and $Ce_{0.6}Zr_{0.4}O_2$ respectively. The values obtained from of the lattice parameter calculation of the solid solutions are: 5.35 ± 0.01 Å and 5.28 ± 0.01 Å for mesoporous $Ce_{0.7}Zr_{0.3}O_2$ and $Ce_{0.6}Zr_{0.4}O_2$ respectively ($CeO_2. = 5.39 \pm 0.01$ Å). No splitting of peaks related to pure CeO_2 or ZrO_2 phase can be observed, which validate the homogeneity and stability of the solid-solution.
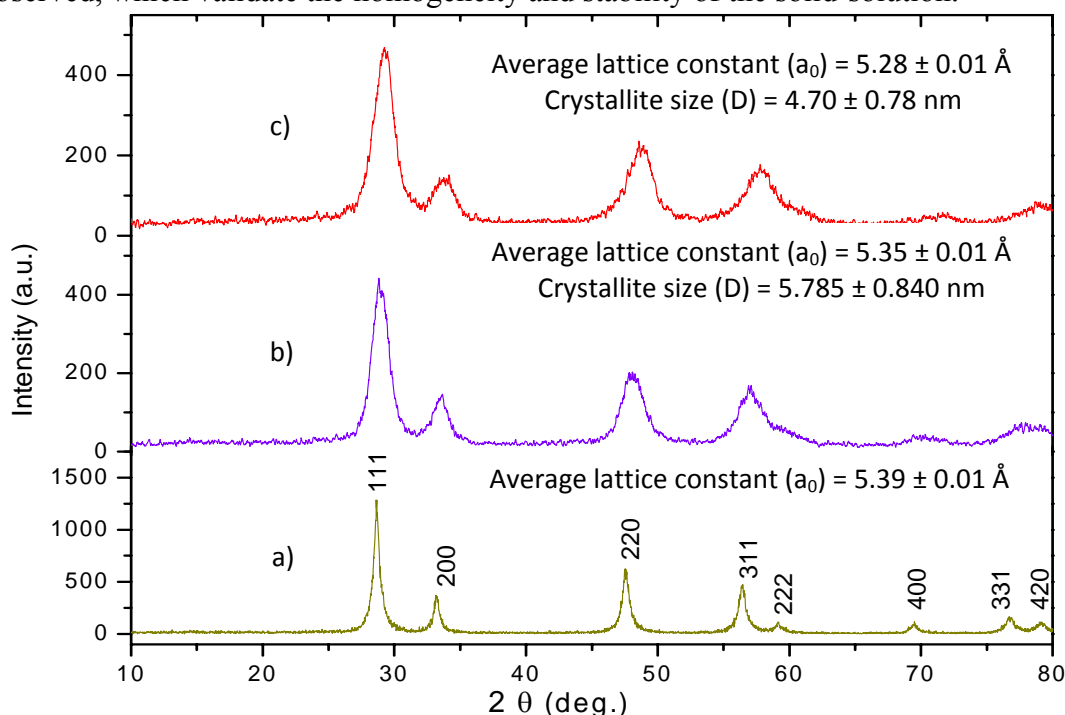
Figure 5.2: XRD patterns of mesoporous: a) CeO_2, b) $Ce_{0.7}Zr_{0.3}O_2$ and c) $Ce_{0.6}Zr_{0.4}O_2$.

In the FT-IR spectrum of mesoporous $Ce_{1-x}Zr_xO_2$ a strong and broad band in the 3500–3400 cm^{-1} region (O-H stretching vibration) and a band at 1630 cm^{-1} (O-H bending vibration) indicated the presence of coordinated water molecules (Figure 5.3 and 5.4), along with the peak at 1386 cm^{-1} indicating O-H bending vibration. The symmetry stretching and asymmetry stretching bands at 2,920 cm^{-1} and 2,850 cm^{-1} of the methyl groups of PEO-block-PPO in the as-synthesized sample is depicted in Figure 5.3a. The spectra at 750 cm^{-1} can be attributed to the presence of Ce-O bond and that at 792 cm^{-1} indicates the presence of Zr-O bond (Figure 5.4b). However, the peaks arising from the surfactant completely disappear after calcinations.

Figure 5.3: The IR spectra of: (a) as-synthesized and (b) calcined $Ce_{1-x}Zr_xO_2$ where x = 0.30
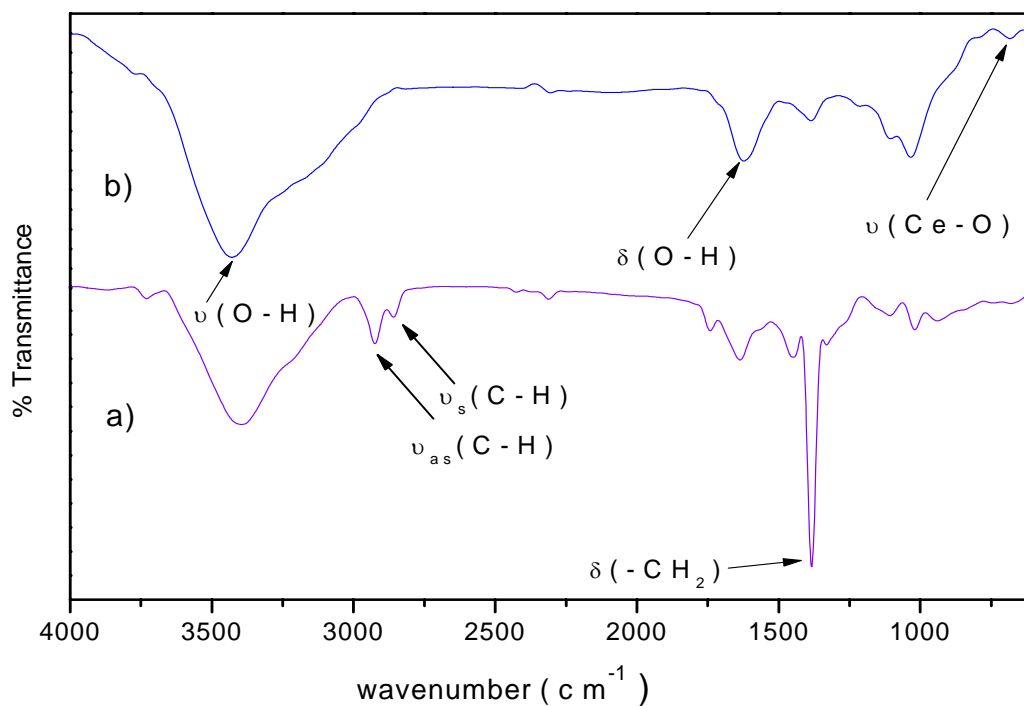
Figure 5.4: The IR spectra of: (a) as-synthesized and (b) calcined $Ce_{1-x}Zr_xO_2$ where x = 0.40.

The N_2 physisorption isotherm of the calcined mesoporous $Ce_{1-x}Zr_xO_2$ where x= 0.3 and 0.4 sample is given in Figure 5.5. The nitrogen sorption isotherms of the samples exhibit a typical

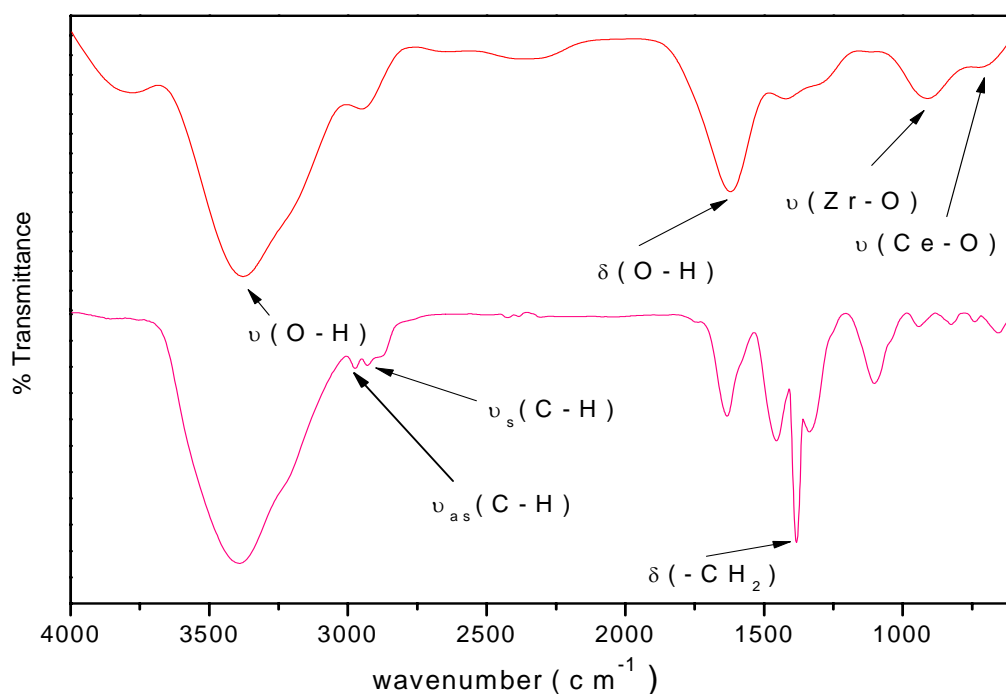type-IV isotherm with a small step and an H4-type hysteretic loop at P/P0 ~ 0.5–0.9, which is the characteristic of mesoporous metal oxides prepared by soft template route. The uptake at high pressure (P/P0~ 0.8–1.0) is associated with the void spaces between the particles. The presences of uni-modal mesopores are confirmed by the PSD which shows a sharp peak at 3.869 nm and 3.19 nm for mesoporous $Ce_{0.7}Zr_{0.3}O_2$ and $Ce_{0.6}Zr_{0.4}O_2$ respectively as depicted in Figure 5.6. The specific BET surface area and the total pore volume of the mesoporous $Ce_{0.7}Zr_{0.3}O_2$ product were found to be 87.839m^2/g and 0.097cm^3/g respectively; for the sample $Ce_{0.6}Zr_{0.4}O_2$ the corresponding values are 79.180 m^2/g and 0.069 cm^3/g respectively.
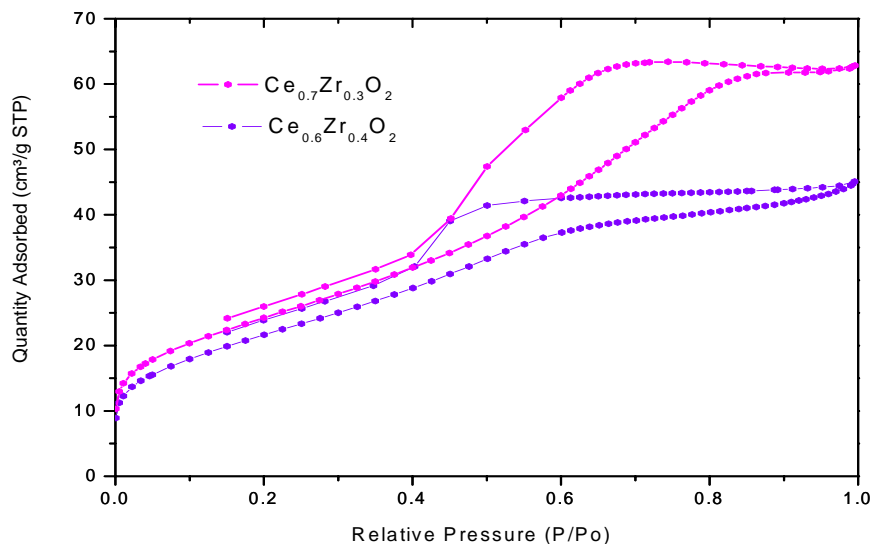
Figure 5.5: N$_2$ sorption isotherms of the mesoporous $Ce_{1-x}Zr_xO_2$ where x= 0.3 and 0.4.
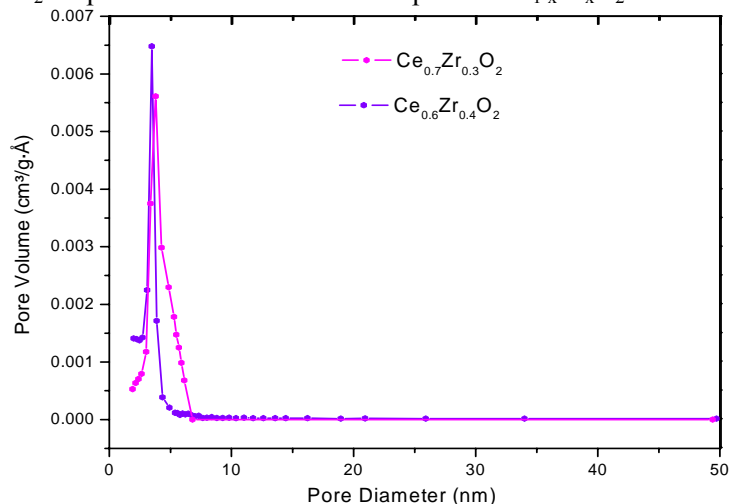
Figure 5.6: Pore size distribution of the mesoporous $Ce_{1-x}Zr_xO_2$ where x= 0.3 and 0.4.

The thermogravimetry and differential thermal analysis (TG-DTA) of the as-synthesized samples were performed (Figure 5.7 and 5.8) .A weight loss of about 25% can be calculated

from TG measurements in the temperature range of 40–200°C. A large obvious peak can also be found in the DTA profile with a large weight loss of about 25% in accordance with the quantity of nitrate in TG curve at about 200°C. It is suggested that the elimination of organic surfactants through combustion generates an exothermic reaction. A large peak in the DTA profile at 350°C corresponds to the loss of surfactant. No peak is found on the DTA curve and no weight loss is observed on the TG curve after 400°C, indicating that the sample has been completely crystallized and all the organics have been removed.
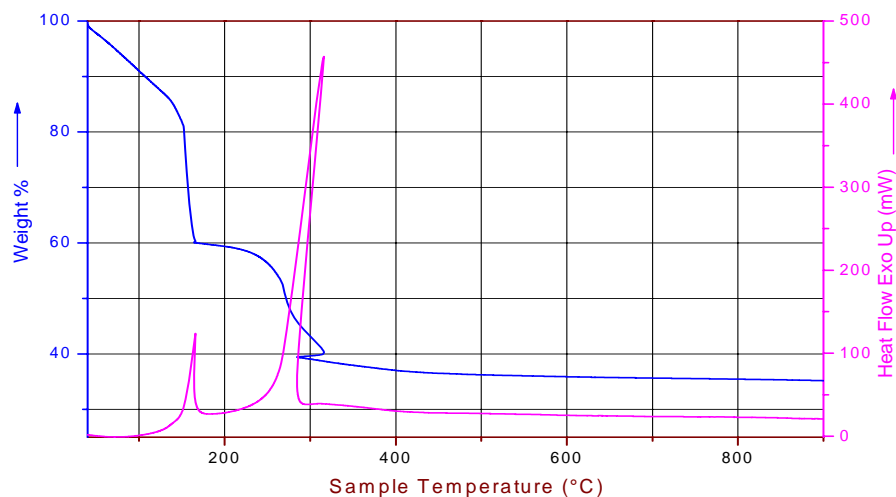
Figure 5.7: TG/DTA of as-synthesized mesoporous $Ce_{1-x}Zr_xO_2$ where x = 0.30
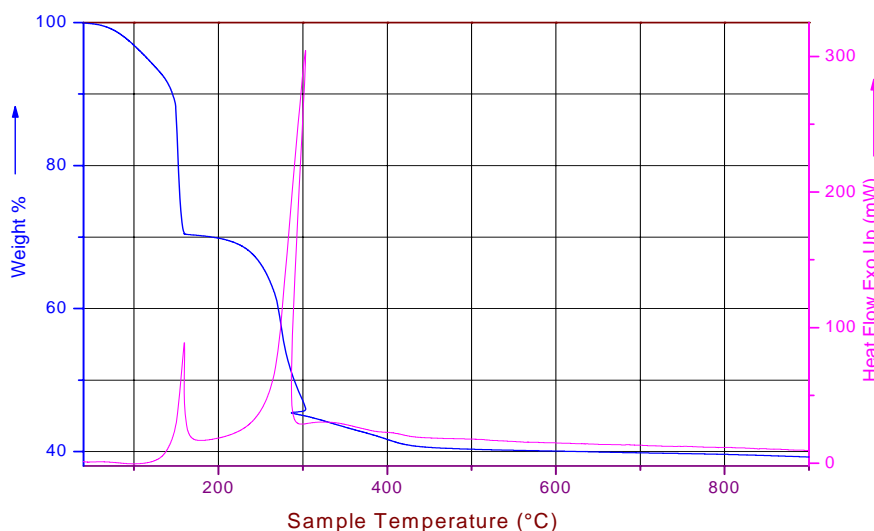
Figure 5.8: TG/DTA of as-synthesized mesoporous $Ce_{1-x}Zr_xO_2$ where x = 0.40

The HRTEM images and corresponding fast Fourier transform (FFT) patterns (Figure 5.9a) reveal a high degree of periodicity for the sample mesoporous $Ce_{0.6}Zr_{0.4}O_2$. The high-resolution

45

TEM (HRTEM) image shows that the walls are highly crystalline. Additional proof for the crystallinity of the framework walls of mesoporous $Ce_{0.6}Zr_{0.4}O_2$ calcined at 400 °C is given by an TEM investigation (Figure 5.9b) that reveals the existence of several nanocrystallites with well-defined lattice planes, which is confirmed by selected-area electron diffraction (SAED, inset of Figure 5.9b). TEM images and corresponding SAED patterns for mesoporous $Ce_{0.7}Zr_{0.3}O_2$ are depicted in Figure 5.10.

Figure 5.9: TEM images of the mesoporous $Ce_{1-x}Zr_xO_2$ (where x = 0.4). The inset in (a) is the corresponding FFT (fast Fourier transform) diffraction image, and the one in (b) is the corresponding SAED pattern.

Figure 5.10: TEM images of the mesoporous $Ce_{1-x}Zr_xO_2$ (where x = 0.3). The inset in (b) is the corresponding SAED pattern.

The morphology of the as-synthesized and calcined mesoporous $Ce_{1-x}Zr_xO_2$ where x = 0.3 and x = 0.4 is analyzed from SEM images (Figure 5.11 and 5.12). Moreover, EDAX analysis

showed the elemental composition of as-synthesized and calcined mesoporous $Ce_{1-x}Zr_xO_2$ where x = 0.3 and x = 0.4 (Figure 5.13 and 5.14).

Figure 5.11: SEM image of: a) as-synthesized and b) calcined mesoporous $Ce_{1-X}Zr_XO_2$ where x= 0.3

Figure 5.12: SEM image of: a) as-synthesized and b) calcined mesoporous$Ce_{1-X}Zr_XO_2$ where x= 0.4

Element	Wt %	At %
O K	22.02	69.41
Zr K	13.06	7.22
Ce L	64.92	23.37

Figure 5.13: EDAX spectrum and elemental quantification of mesoporous $Ce_{1-X}Zr_XO_2$ where x= 0.3.
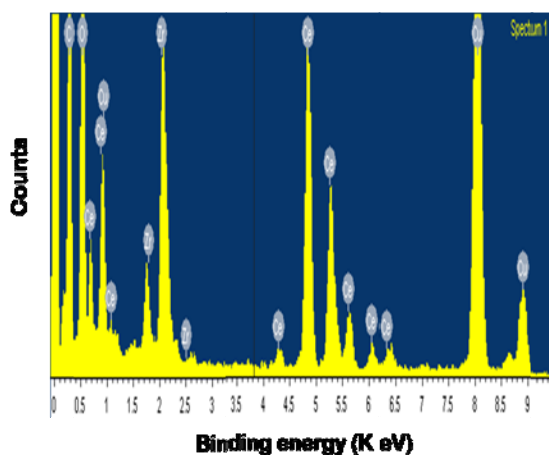
Element	Wt %	At %
O K	26.36	73.62
Zr K	17.01	8.33
Ce L	56.62	18.05

Figure 5.14: EDAX spectrum and elemental quantification of mesoporous $Ce_{1-X}Zr_XO_2$ where x= 0.4.

5.3.2. Characterization of mesoporous $Zr_{1-x}Ce_xO_2$; x = 0.3 and 0.4.

The low angle XRD patterns of the calcined mesoporous $Zr_{0.7}Ce_{0.3}O_2$ and $Zr_{0.6}Ce_{0.4}O_2$ are shown in Figure 5.15. The mesostructured long range ordering of the composite was confirmed by low-angle XRD. Low-angle XRD pattern, exhibits a single well-resolved diffraction peak corresponding to (100) plane, which are characteristics of a 2D hexagonal (*p6mm*) structure.

Figure 5.15: Small angle XRD patterns of mesoporous a) $Zr_{0.7}Ce_{0.3}O_2$ and b) $Zr_{0.6}Ce_{0.4}O_2$.

The high-angle XRD patterns of the calcined mesoporous $Zr_{0.7}Ce_{0.3}O_2$ and $Zr_{0.6}Ce_{0.4}O_2$ calcined at 673 K is shown in Figures 5.16a and b respectively. The XRD patterns of mesoporous $Zr_{1-x}Ce_xO_2$ is indicative of well-crystallized inorganic frameworks corresponding to the crystalline cubic fluorite phase. According to the Scherrer equation, the crystallite size of calcined samples are 8.9 ± 1.4 nm nm and 10.2 ± 1.8 nm for mesoporous $Zr_{0.7}Ce_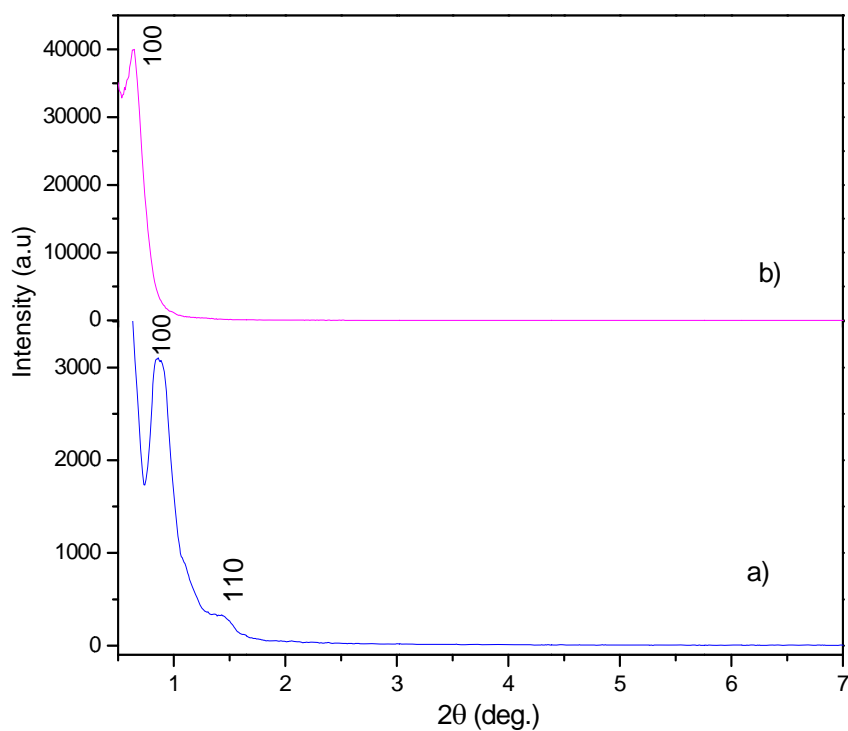{0.3}O_2$ and $Zr_{0.6}Ce_{0.4}O_2$ respectively. The calculated value of the lattice parameter of the solid solutions are: 5.21 ± 0.01 Å and 5.25 ± 0.01 Å for mesoporous $Zr_{0.7}Ce_{0.3}O_2$ and $Zr_{0.6}Ce_{0.4}O_2$ respectively (CeO_2 = 5.399 ± 0.009 Å).   No splitting of peaks related to pure CeO_2 or ZrO_2 phase can be observed, which validate the homogeneity and stability of the solid-solution
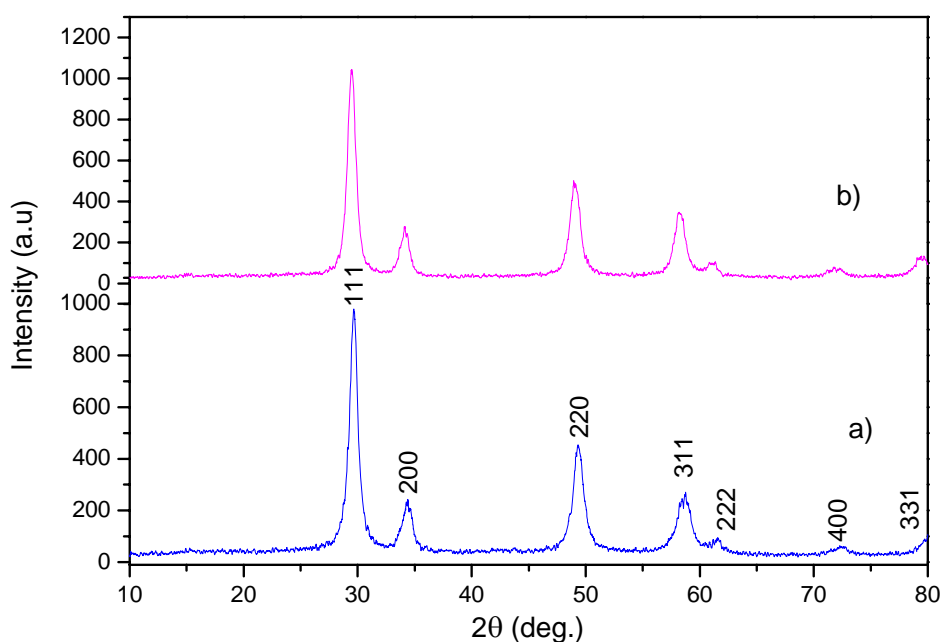
Figure 5.16: XRD patterns of mesoporous : a) $Zr_{0.7}Ce_{0.3}O_2$ and b) $Zr_{0.6}Ce_{0.4}O_2$.

In the FT-IR spectrum of mesoporous $Zr_{1-X}Ce_XO_2$ a strong and broad band in the 3500–3400 cm^{-1} region (O-H stretching vibration) and a band at 1630 cm^{-1} (O-H bending vibration) indicated the presence of coordinated water molecules (Figure 5.17 and 5.18), along with the peak at 1386 cm^{-1} indicating O-H bending vibration. The symmetry stretching and asymmetry stretching bands at 2,920 cm^{-1} and 2,850 cm^{-1} of the methyl groups of PEO-block-PPO in the as-synthesized sample is depicted in Figure 5.17a. The spectra at 750 cm^{-1} can be attributed to the presence of Ce-O bond and that at 792 cm^{-1} indicates the presence of Zr-O bond (Figure 5.18b). However, the peaks arising from the surfactant completely disappear after calcinations.
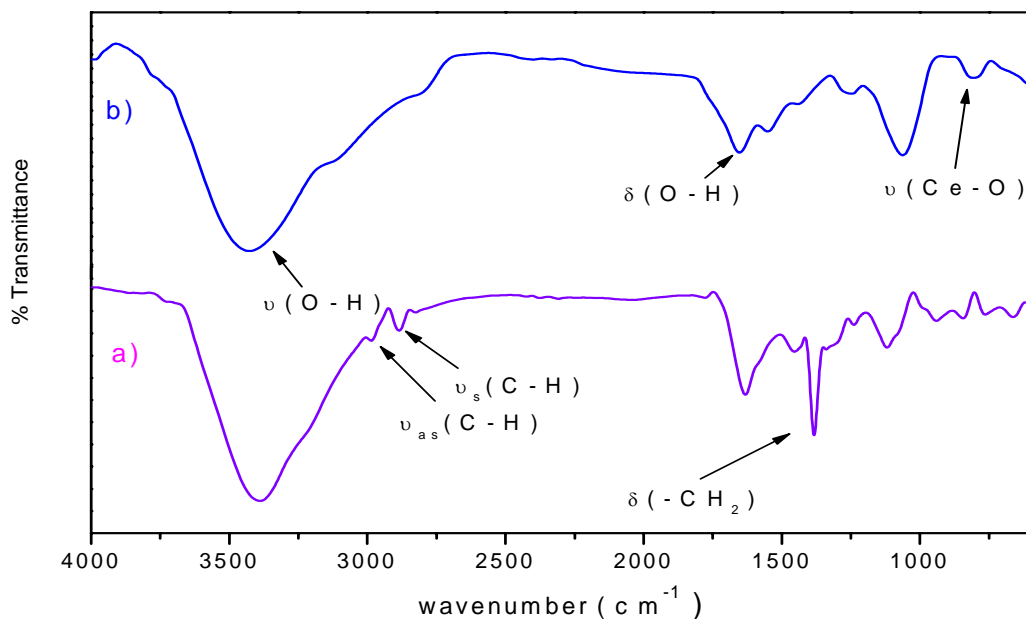
Figure 5.17: The IR spectra of: (a) as-synthesized and (b) calcined $Zr_{1-X}Ce_XO_2$ where x = 0.30
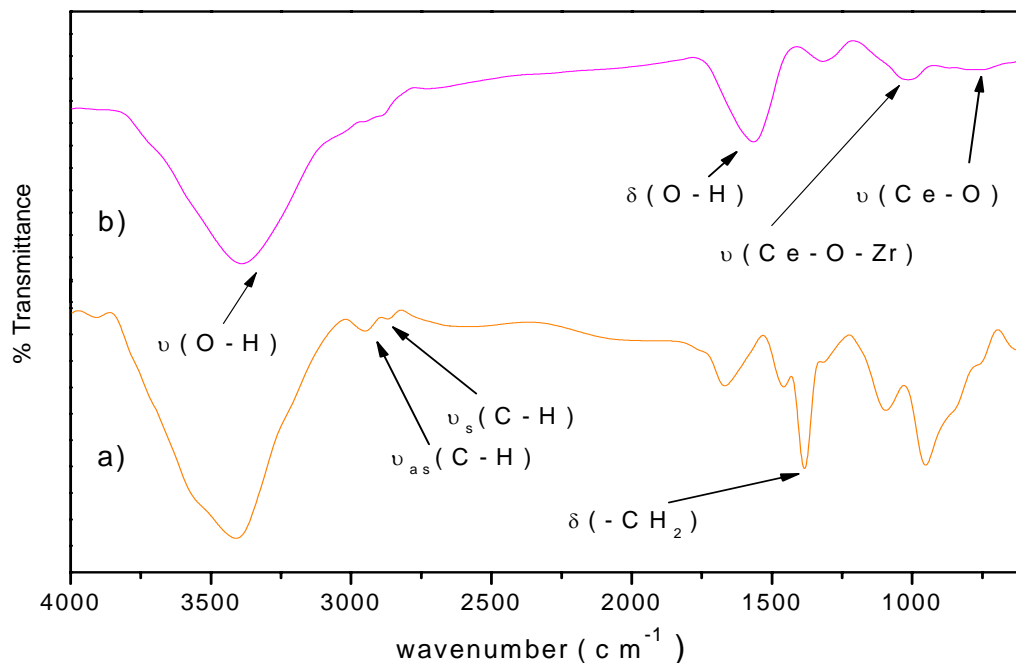
Figure 5.18: The IR spectra of: (a) as-synthesized and (b) calcined $Zr_{1-X}Ce_XO_2$ where x = 0.40

The N_2 physisorption isotherm of the calcined mesoporous $Zr_{1-x}Ce_xO_2$ where x= 0.3 and 0.4 sample is given in Figure 5.19. The nitrogen sorption isotherms of the samples exhibit a typical type-IV isotherm with a small step and an H4-type hysteretic loop at P/P0 ~ 0.4–0.9, which is the characteristic of mesoporous metal oxides prepared by soft template route. The presences of uni-

modal mesopores are confirmed by the PSD which shows a sharp peak at 4.613 nm and 3.23 nm for mesoporous $Zr_{0.7}Ce_{0.3}O_2$ and $Zr_{0.6}Ce_{0.4}O_2$ respectively as depicted in Figure 5.20. The specific BET surface area and the total pore volume of the mesoporous $Zr_{0.7}Ce_{0.3}O_2$ product were found to be $46.507 m^2/g$ and $0.077 cm^3/g$ respectively ; for the sample $Zr_{0.6}Ce_{0.4}O_2$ the corresponding values are $50.57 m^2/g$ and $0.048 cm^3/g$ respectively.
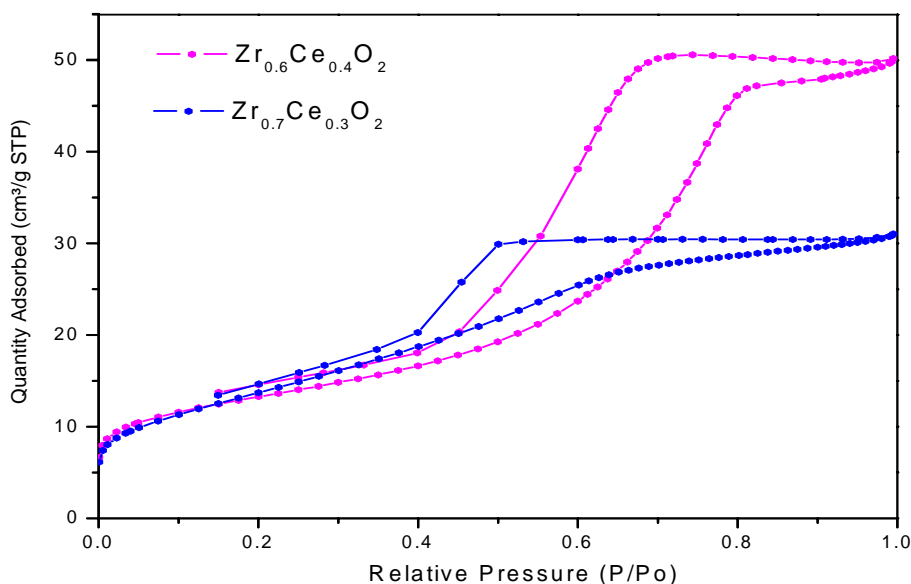
Figure 5.19: N₂ sorption isotherms of the mesoporous $Zr_{1-X}Ce_XO_2$ where x= 0.3 and 0.4.
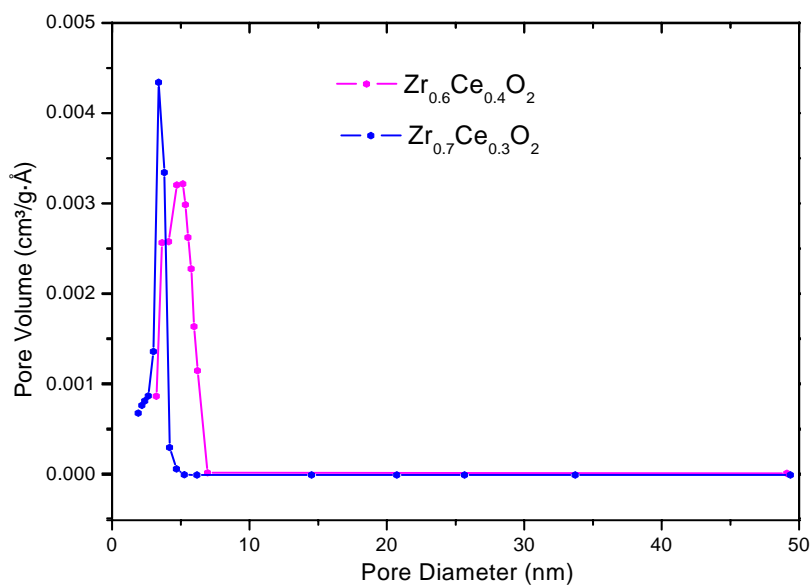
Figure 5.20: Pore size distribution of the mesoporous $Zr_{1-X}Ce_XO_2$ where x= 0.3 and 0.4.

The TG-DTA of the as-synthesized sample was performed at a linear heating rate of 10°C/min. TG analysis (Figure 5.21 and 5.22) was performed to determine the complete conversion temperature of nitrate precursor. A weight loss of about 20% can be calculated from TG measurements in the temperature range of 40–200°C. A large obvious peak can also be found in the DTA profile with a large weight loss of about 20% in accordance with the quantity of nitrate in TG curve at about 200°C. It is suggested that the elimination of organic surfactants through combustion generates an exothermic reaction. A large peak in the DTA profile at 350°C corresponds to the loss of surfactant.
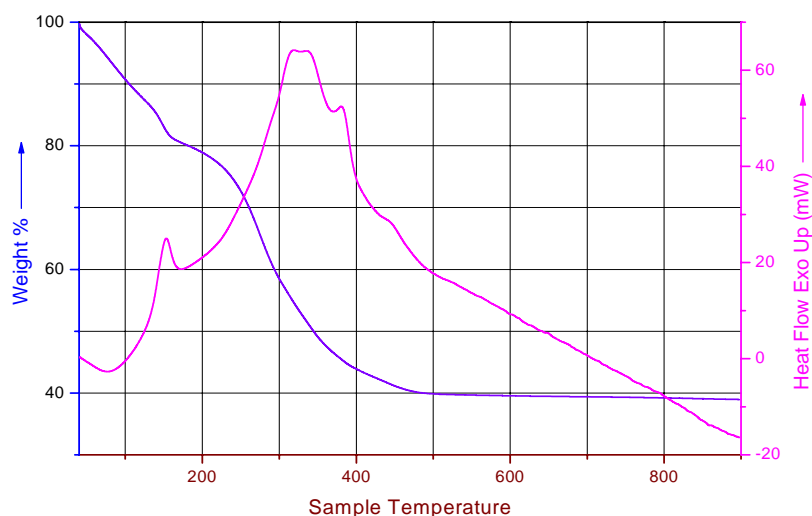
Figure 5.21: TG/DTA of as-synthesized mesoporous $Zr_{1-X}Ce_XO_2$ where x = 0.30.
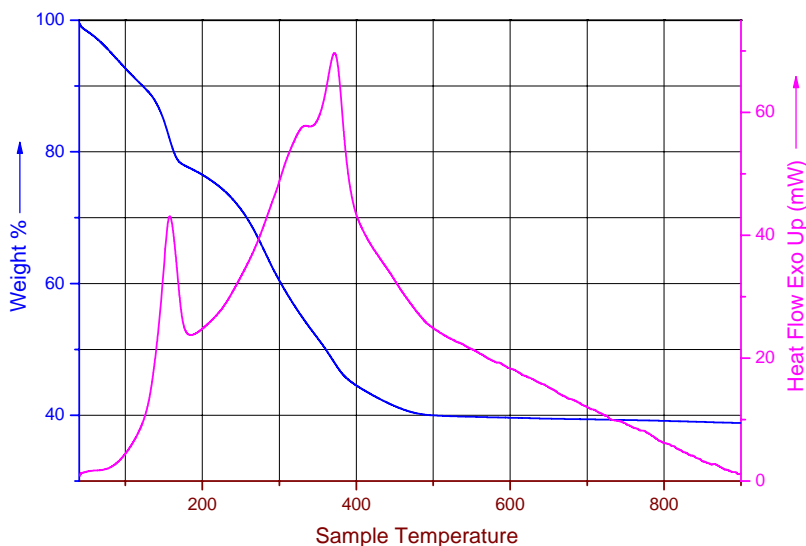
Figure 5.22: TG/DTA of as-synthesized mesoporous $Zr_{1-X}Ce_XO_2$ where x = 0.40

52

The HRTEM images and corresponding fast Fourier transform (FFT) patterns (Figure 5.23a) reveal a high degree of periodicity for the sample mesoporous $Zr_{0.7}Ce_{0.3}O_2$. The high-resolution TEM (HRTEM) image shows that the walls are highly crystalline. Additional proof for the crystallinity of the framework walls of mesoporous $Zr_{0.7}Ce_{0.3}O_2$ calcined at 400 °C is given by an TEM investigation (Figure 5.23b) that reveals the existence of several nanocrystallites with well-defined lattice planes, which is confirmed by selected-area electron diffraction (SAED, inset of Figure 5.23b). TEM images and corresponding SAED patterns for mesoporous $Zr_{0.6}Ce_{0.4}O_2$ are depicted in Figure 5.24.
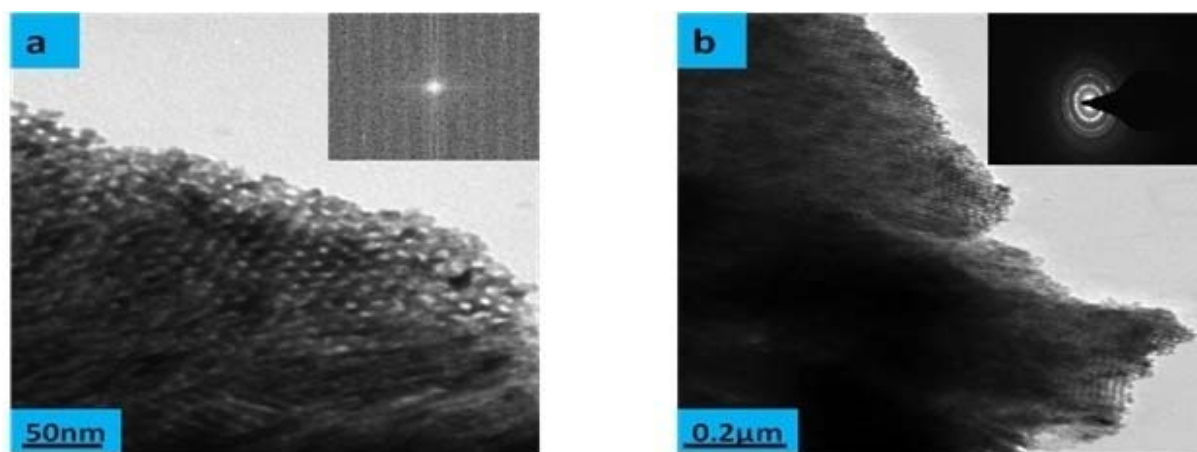
Figure 5.23: TEM of the mesoporous $Zr_{1-X}Ce_XO_2$ (where x = 0.3). The inset in (a) is the corresponding FFT (fast Fourier transform) diffraction image, and the one in (b) is the corresponding SAED pattern.
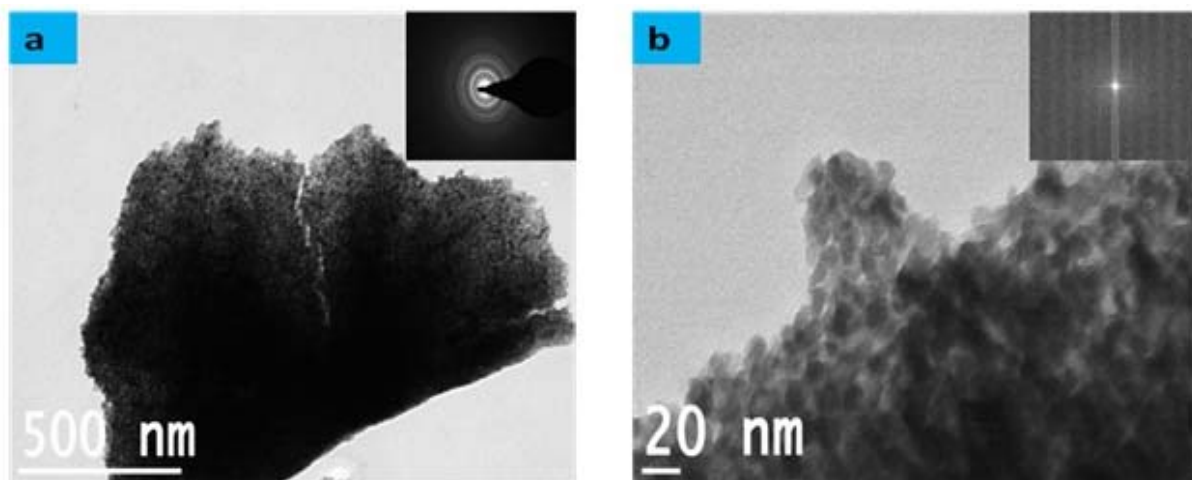
Figure 5.24: TEM of the mesoporous $Zr_{1-X}Ce_XO_2$ (x = 0.4). The inset in (a) is the corresponding SAED pattern; (b) is the corresponding FFT diffraction image.

53

The morphology of the as-synthesized and calcined mesoporous $Zr_{1-X}Ce_XO_2$ where x = 0.3 and x = 0.4 is analyzed from SEM images (Figure 5.25 and 5.26). Moreover, EDAX analysis showed the elemental composition of as-synthesized and calcined mesoporous $Zr_{1-X}Ce_XO_2$ where x = 0.3 and x = 0.4 (Figure 5.27 and 5.28).
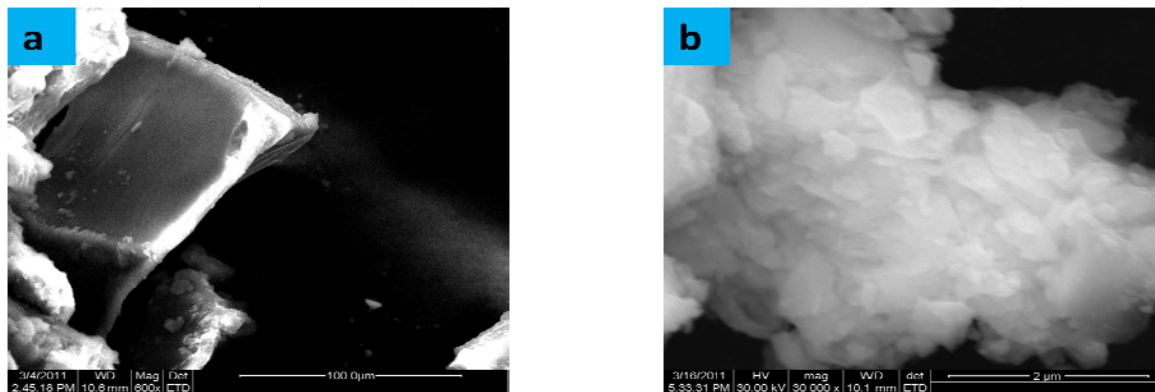
Figure 5.25: SEM image of: a) as-synthesized and b) calcined mesoporous $Zr_{1-X}Ce_XO_2$ where x= 0.3
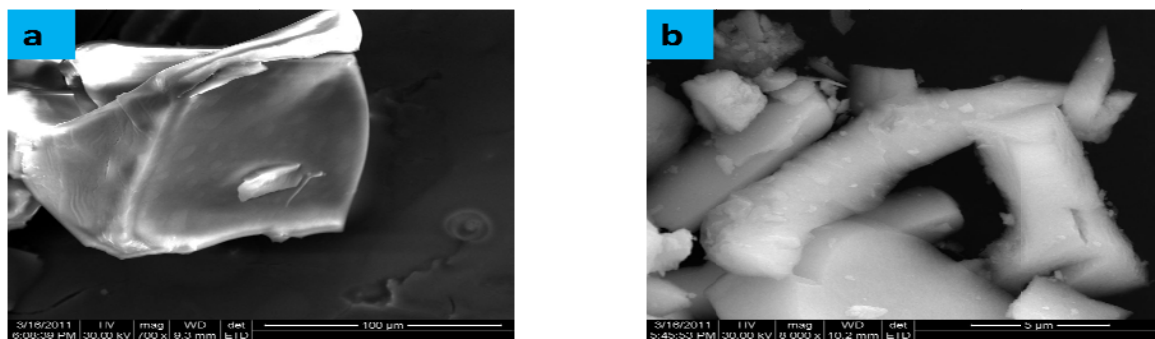
Figure 5.26: SEM image of: a) as-synthesized and b) calcined mesoporous $Zr_{1-X}Ce_XO_2$ where x= 0.4

Element	Wt %	At %
O K	25.09	68.06
Cl K	00.86	01.05
Ce L	26.14	08.10
Zr K	47.92	22.80
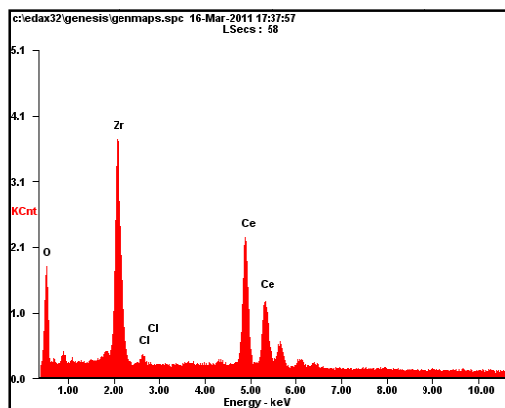
Figure 5.27: EDX spectrum and elemental quantification of mesoporous $Zr_{1-X}Ce_XO_2$ where x= 0.3
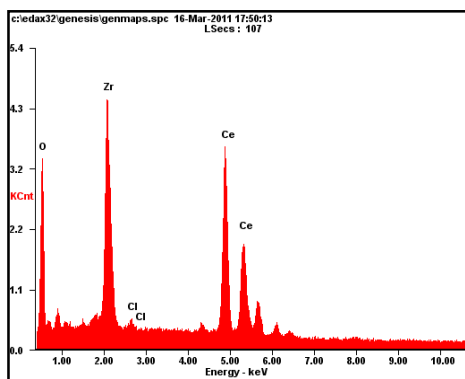
Element	Wt %	At %
O K	25.09	68.06
Cl K	00.86	01.05
Ce L	26.14	08.10
Zr K	47.92	22.80

Figure 5.28: EDX spectrum and elemental quantification of mesoporous $Zr_{1-X}Ce_XO_2$ where x= 0.4

Table 5.1: Synopsis of Textural Properties of Mesoporous Ceria-Zirconia Solid Composite.

Mesoporous Sample	d_{100} (nm)	Lattice Cell Parameter a_o (Å)	BET surface area (m²/g)	Pore volume (cm³/g)	Avg. Pore size (Å)
$Ce_{0.7}Zr_{0.3}O_2$	13.5	5.345	87.84	0.097	3.869
$Ce_{0.6}Zr_{0.4}O_2$	13.2	5.280	79.18	0.069	3.19
$Zr_{0.6}Ce_{0.4}O_2$	13.9	5.246	46.50	0.077	4.61
$Zr_{0.7}Ce_{0.3}O_2$	10.2	5.212	50.57	0.048	3.23

According to Vegard's rule, due to the smaller Zr^{4+} ionic radius (0.84Å) compared to that of Ce^{4+} (0.97Å) , a linear decrease of the lattice cell parameter is expected to occur upon insertion of increasing amounts of ZrO_2 into the CeO_2 lattice. Partial reduction of Ce^{4+} to Ce^{3+} significantly contribute to enhance the cationic mobility in the lattice and also expands the lattice, thus allowing the solid solution to be attained. Figure 15 shows the variation of lattice constant in mesoporous $Ce_{1-X}Zr_XO_2$ solid solution samples calcined at 400°C as a function of Zr content 'x'.
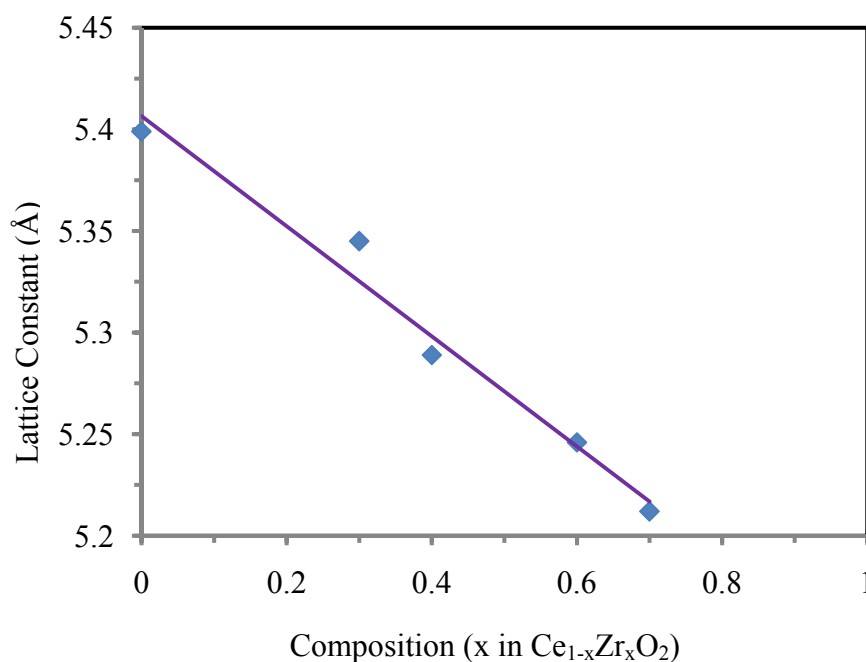
Figure 5.29: Lattice constant of mesoporous $Ce_{1-x}Zr_xO_2$ as a function of Zr content 'x'.

5.4 CONCLUSION

In summary, a facile and widely applicable EISA method was exploited for the synthesis of ceria-zirconia solid solutions with highly ordered mesoporous structures from the combination of tri-block co-polymers with metal inorganic salts solubilized in ethanol solution. Herein, all of the hydrolysis, condensation, and assembly processes are self-adjusting without additional acid or base. Pure ceria-zirconia solid solutions with well organized pore structures are all obtained via this facile synthesis method. The mesoporous materials above have large surface areas, tunable pore sizes, crystalline frameworks, multiple components, a high degree of homogeneity and thermally stable which presents advantages for commercial applications in heterogeneous catalysts and oxygen sensors. Most importantly, using this "self-adjusting" method, the diverse hydrolysis-condensation kinetics of the two metal oxides ceria and zirconia is homogenized. The development of such a simple and widely applicable method for the fabrication of novel mesoporous functional materials with diverse compositions is important for practical applications. in catalysis.

CHAPTER 6

SUMMARY

Mesoporous Ceria was prepared by both chemical soft templating and nanocasting method. Template removal process (NaOH leaching) had been optimized in case of replica method for tuning the textural and morphological features of the mesoporous ceria. The prepared metal oxide is the reverse replica of the hard template SBA-15 and has long range order with hexagonal symmetry, which was further confirmed by the TEM images. Mesoporous ceria with crystalline pore walls and large specific surface area (143.86   m²/g) was obtained using ethanolic solution of $Ce(NO_3)_3$ as the precursor and two times impregnation step was performed in order to fill the porosities to the highest possible level. Meanwhile, mesopore sizes obtained from the nanocasting process are relatively small and not easy tunable because these mesopores originated from the mesoporous silica walls whose thickness is difficult to control. For retaining mesostucture in case of co-operative self-assembly process, the ethanol extraction technique which is an optimum method for removing non ionic surfactant was utilized. Finally, nanocasting method was found to be the best method for preparing mesoporous ceria so far as the textural properties of the prepared oxide were concerned.

Mesostructured zirconia having good microtexture was prepared via cooperative self assembly mechanism of the so called chemical soft templating method combined with block-copolymer P123 as structure-directing agent. Also adopting tis procedure both tetragonal and thermodynamically more favorable monoclinic phases of zirconia was successfully prepared by varying the synthesis parameters such as Zr/OH^- molar ratio and crystal lization temperature. Template removal process had been optimized for both nanocasting and soft-templating approach. Although mesoporous zirconia can be prepared using either silica or P123 as the templates, the different preparation methods might result in zirconia possessing different surface micro-environments, simply because the removal process of templates is different. Mesoporous ZrO_2 prepared via the replica method with SBA-15 as the hard template had the same rope-like domains and p6mm symmetry as the parent SBA-15. But some residual silicon remained in the mesoporous ZrO_2 which was found to stabilise the tetragonal phase of ZrO_2. Although replica

method itself was successfully applied to prepare ordered mesoporous ZrO_2, but that mesoporous silica is not the appropriate hard template because Si cannot be removed completely from the product.

The liquid crystal templating approach was exploited for the synthesis of ceria-zirconia solid solutions with highly ordered mesoporous structures. Pure ceria-zirconia solid solutions with well organized pore structures and high specific surface areas are all obtained via this EISA method. All of the hydrolysis, condensation, and assembly processes are self-adjusting without additional acid or base. The structural characteristics of mesoporous ceria- zirconia solid composite have been systematically investigated. SAED patterns show the atomic-scale crystallinity of the prepared material. The TEM and FFT analyses confirm the presence of well defined hexagonal arrangements of the pore channels in mesoporous $Zr_{0.7}Ce_{0.3}O_2$ .Thus the use of various spectroscopic and non-spectroscopic techniques provided interesting information regarding the physicochemical characteristics of and mesoporous ceria-zirconia composite.

REFERENCES

1. **Blin, J. L., R. Flamant** and **B. L. Su** (2001) Synthesis of nanostructured mesoporous zirconia using CTMABr– $ZrOCl_2$.$8H_2O$ systems: a kinetic study of synthesis mechanism. *Int. J. Inorg. Mater.*, **3**, 959–972.

2. **Boaro, M., M. Vicario, C. Leitenburg, G. Dolcetti** and **A. Trovarelli** (2003) The use of temperature-programmed and dynamic/transient methods in catalysis: characterization of ceria-based, model three-way catalysts. *Catal. Today*, **77**, 407–417.

3. **Brezesinski, T., M. Antonietti, M. Groenewolt, N. Pinna** and **B. Smarsly** (2005) The generation of mesostructured crystalline CeO_2, ZrO_2 and CeO_2-ZrO_2 films using evaporation-induced self-assembly. *New J. Chem.,* **29**, 237–242.

4. **Brezesinski, T., M. Groenewolt, A. Gibaud, N. Pinna, M. Antonietti,** and **B. M. Smarsly (**2006) Evaporation-induced self-assembly (EISA) at its limit:Ultrathin, crystalline patterns by templating of micellar monolayers. *Adv. Mater.*, **18**, 2260–2263.

5. **Brinker, C. J., Y. Lu, A. Sellinger** and **H. Fan** (1999) Evaporation-induced self-assembly: nanostructures made easy. *Adv. Mater.*, **11**, 579–585.

6. **Cagnol, F., D. Grosso, G. J. de A. A. Soler-Illia, E. L. Crepaldi, F. Babonneau, H. Amenitsch,** and **C. Sanchez** (2003) Humidity-controlled mesostructuration in CTAB-templated silica thin film processing. The existence of a modulable steady state. *J. Mater. Chem.,* **13**, 61–66.

7. **Carreon, M. A.** and **V. V. Guliants** (2005) Ordered meso and macroporous binary and mixed metal oxides. *Eur. J. Inorg. Chem.*, **1**, 27–43.

8. **Ciesla, U., M. Froba, G. Stucky** and **F. Schuth** (1999) Highly Ordered Porous Zirconias from Surfactant-Controlled Syntheses: Zirconium Oxide-Sulfate and Zirconium Oxo. *Chem. Mater.,* **11**, 227-234.

9. **Das, S. K., M. K. Bhunia, A. K. Sinha** and **A. Bhaumik** (2009) Self-Assembled Mesoporous Zirconia and Sulfated Zirconia Nanoparticles Synthesized by Triblock Copolymer as Template. *J. Phys. Chem. C*, **113**, 8918–8923.

10. **Ernst, S.** *Advances in Nanoporous Materials.*Vol1. Elsvier Press, UK, 2009.

11. **Ghom, S. A., C. Zamani, S. Nazarpour** and **T. Andreu** (2009) Oxygen sensing with mesoporous ceria–zirconia solid solutions. *Sens. Actuators, B,* **140**, 216–221.

12. **Grosso, D., F. Cagnol, G. J. de A. A. Soler-Illia, E. L. Crepaldi, H. Amenitsch, A. Brunet-Bruneau, A. Burgeois** and **C. Sanchez** (2004) Fundamentals of mesostructuring through evaporation-induced self-assembly. *Adv. Funct. Mater,* **14**, 309–322.

13. **Guliants, V. V., M. A. Carreon** and **J. Y,Lin** (2004) Ordered mesoporous and macroporous inorganic films and membranes'' *J. Membr. Sci*., **235**, 53–72.

14. **He, X.** and **D. Antonelli** (2002) Recent Advances in Synthesis and Applications of Transition Metal Containing Mesoporous Molecular Sieves. *Angew. Chem. Int. Ed.,* **41**, 214–229.

15. **Hurd, A. J**. and **L. Steinberg** (2001) The physics of evaporation-induced assembly of sol-gel materials. *Granular Matter*, **3**, 19–21.

16. **Jasinski, P., T. Suzuki** and **H. U.Anderson** (2003) Nanocrystalline undoped ceria oxygen sensor. *Sens. Actuators B*, **95**, 73–77.

17. **Kleitz, F., S. J. Thomson, Z. Liu** and **O. Terasaki** (2002) Porous Mesostructured Zirconium Oxophosphate with Cubic (Ia3hd) Symmetry. *Chem. Mater.,* **14**, 4134-4144.

18. **Li, Y.** and **L. Luo** (2009) Study on the synthesis of mesoporous ceria in the presence of glucose and acrylamide. *J. Chil. Chem. Soc.,* **54**, 168 -170.

19. **Liu, B.** and **R. T**. **Baker** (2008) Factors affecting the preparation of ordered mesoporous ZrO_2 using the replica method. *J. Mater. Chem.,* **18**, 5200–5207.

20. **Liu, X. M., Z. F**. **Yan** and **M. G. Q. Lu** (2008) Solid-state synthesis and characterisation of mesoporous zirconia with lamellar and wormhole-like mesostructures. *J. Porous Mater,* **15**, 237-244.

21. **Lu, Y., H. Fan, N. Doke, D. A. Loy, R. A. Assink, D. A. LaVan** and **C. J. Brinker** (2000) Evaporation Induced self-assembly of hybrid bridged silsesquioxane film and particulate mesophases with integral organic functionality. J. Am. Chem. Soc., **122**, 5258–5261.

22. **Lyons, D. M., K. M. Ryan** and **M. A. Morris** (2002) Preparation of ordered mesoporous ceria with enhanced thermal stability. *J. Mater. Chem.,* **12**, 1207–1212.

23. **Lyu, Y. Y., S. H. Yi, J. K. Shon, S.Chang, L. S. Pu, S.Y. Lee , J. E. Yie, K. Char, G. D. Stucky** and **J. M. Kim** (2004) Highly Stable Mesoporous Metal Oxides Using Nano-Propping Hybrid Gemini Surfactants. *J. Am. Chem. Soc.,* **126**, 2310-2311.

24. **Madier, Y., C. Descorme, A. M. Le Govic,** and **D. Duprez** (1999) Oxygen Mobility in CeO_2 and $Ce_xZr_{(1-x)}O_2$ Compounds: Study by CO Transient Oxidation and $^{18}O/^{16}O$ Isotopic Exchange . *Phys. Chem. B*., **103 (50)**, 10999–11006.

25. **Pacheco, G., E. Zhao, A. Garcia, A**. **Sklyarov** and **J. J. Fripiat** (1998) Synthesis of mesoporous zirconia with anionic surfactants. *J. Mater. Chem.*, **8(1)**, 219–226.

26. **Parida, K. M., S. Mallick, P. C. Sahoo** and **S. K. Rana** (2010) A facile method for synthesis of amine-functionalized mesoporous zirconia and its catalytic evaluation in Knoevenagel condensation. *Appl. Catal., A,* **381**, 226–232.

27. **Sobukawa, H.** (2002) Development of Ceria Zirconia solid solution and Future trends. *R& D Review of Toyota CRDL*, **37(4)**

28. **Soler-Illia, G. J. A. A., C. Sanchez, B. Lebeau** and **J.Patarin** (2002) Chemical Strategies To Design Textured Materials: from Microporous and Mesoporous Oxides to Nanonetworks and Hierarchical Structures. *Chem. Rev*., **102**, 4093–4138.

29. **Soler-Illia, G. J. de A. A., E. L. Crepaldia, D. Grossoa** and **C. Sanchez** (2003) Block copolymer-templated mesoporous oxides. *Curr. Opin. Colloid Interface Sci*., **8,** 109–126.

30. **Suzuki, Z. K**. and **A. K. Sinha** (2007) Monodisperse, bimodal mesoporous ceria catalysts and adsorbents for air purification. *J. Mater. Chem.,* **17**, 2547–2551.

31. **Trovarelli, A.** *Catalysis by Ceria and related Materials*. Imperial College Press, London, 2002.

32. **Vartuli, J. C., C. T. Kresge, M. E. Leonowicz, A. S. Chu, S. B. McCullen, I. D. Johnson** and **E. W.Sheppard (**1994) Synthesis of mesoporous materials: liquid-crystal templating versus intercalation of layered silicates. *Chem. Mater*., **6**, 2070–2077.

33. **Wan, Y.** and **D. Zhao** (2007) On the Controllable Soft-Templating Approach to Mesoporous Silicates. Chem Rev., **107(7)**, 2821-2860.

34. **Wang, J. A., M. A. Valenzuela, J. Salmones** and **A. Vázquez** (2001) Comparative study of nanocrystalline zirconia prepared by precipitation and sol–gel methods. *Catal. Today*, **68**, 21–30.

35. **Wang, Y., Y.Wang, J. Ren, Y. Mi, F. Zhang, C. Li, X. Liu, Y. Guo, Y. Guo** and **G. Lu** (2010) Synthesis of morphology-controllable mesoporous Co_3O_4 and CeO_2. *J. Solid State Chem.*, **183**, 277–284.

36. **Yang, P., D. Zhao, D. I. Margolese, B. F.Chmelka** and **G. D.Stucky** (1998) Generalized syntheses of large-pore mesoporous metal oxides with semicrystalline frameworks. *Nature,* **396**, 152–155.

37. **Yuan, Q., L.L. Li, S.L. Lu, H.H. Duan, Z.X. Li, Y.X. Zhu** and **C.H. Yan** (2009). Facile Synthesis of Zr-Based Functional Materials with Highly Ordered Mesoporous Structures. *J. Phys. Chem. C*, **113**, 4117–4124.

38. **Yue, L.** and **X.M. Zhang** (2009) Texture stability of mesoporous ceria made nanoparticles assembly. *Ceram. Int.,* **35**, 847–853.

39. **Zhang, G., Z. Shen, M. Liu, C. Guo, P. Sun, Z. Yuan, B. Li, D. Ding** and **T. Chen** (2006) Synthesis and Characterization of Mesoporous Ceria with Hierarchical Nanoarchitecture Controlled by Amino Acids. *J. Phys. Chem. B,* **110**, 25782-25790.

40. **Zhao, X. B., F. Chen, J. You, X. Z. Li, X. W. Lu** and **Z. G. Chen** (2010) The synthesis of mesoporous $Ce_{1-2x}Zr_xO_2$ by modified evaporation-induced self-assembly method. *J. Mater. Sci.,* **45**, 3563–3568.